Interlaken - Schloss (SINS)
SITE CHARACTERIZATION REPORT

Clotaire MICHEL, Valerio POGGI, Daniel ROTEN,

Jan BURJANEK, Carlo CAUZZI, Donat FÄH

Sonneggstrasse 5 CH-8092 Zürich Switzerland; E-mail: clotaire.michel@sed.ethz.ch

Last modified : November 5, 2013

1

Abstract

Ambient vibration array measurements were performed to characterize the lacustrine deposits at site Interlaken Schloss. The site, where the new station SINS of the Swiss Strong Motion Network was installed, is located in the eastern part of Interlaken city, in the castle. In order to characterize the velocity profile under the station, 2 array measurements with 80 and $450\,\mathrm{m}$ aperture were performed. The measurements were successful and allowed deriving a velocity model for this site. The soil column underlying station SINS is made of 3 meters that show low velocity values and a first layer down to $30\,\mathrm{m}$ depth with relatively homogeneous velocity ($300\,\mathrm{m/s}$). At this depth, a clear interface with a layer with a $450\,\mathrm{m/s}$ velocity is found down to 130 to $150\,\mathrm{m}$ depth. At this depth, it increases up to $750\,\mathrm{m/s}$ in a layer that is found down to the bedrock with slightly increasing velocity, at $380\,\mathrm{m}$ depth, according to geophysical and geomorphological constraints. The basin is found to be working on a 2D resonance mode, with a fundamental SH frequency of $0.51\,\mathrm{Hz}$.

$V_{s,30}$ is $266\,\mathrm{m/s}$, which corresponds to ground type C in the Eurocode 8 [CEN, 2004] and class D in SIA261 [SIA, 2003]. The theoretical 1D SH transfer function and impedance contrast of the quarter-wavelength velocity computed from the inverted profiles show large amplifications at resonance frequencies over a broad frequency range, but the 2D behavior may have a strong impact on this. Recordings on the new station will allow to compare to these simple models.

Contents

1   Introduction

The station SINS (Interlaken - Schloss) is part of the Swiss Strong Motion Network (SSM-Net) in Berner Oberland. SINS has been installed in the framework of the SSMNet Renewal project in 2012 as a new site. This project includes also the site characterization. Passive array measurements have been selected as a standard tool to investigate these sites. Such a measurement campaign was carried out on 21st August 2012 in the Höhematte field and close to the castle (Fig. 1), with a centre at station SINS, in order to characterize the sediments under this station. Moreover, a H/V campaign was carried out in the whole city in order to evaluate variations in the bedrock depth. According to the geological map, this station is located on loose glacial-lacustrine sediments of the Aare basin inbetween lake Thun and lake Brienz. This report presents the measurement setup, the results of the H/V analysis and of the array processing of the surface waves (dispersion curves). Then, an inversion of these results into velocity profiles is performed. Standard parameters are derived to evaluate the amplification at this site.

Canton	City	Location	Station code	Site type	Slope
Bern	Interlaken	Schloss	SINS	Lacustrine plain	Flat

Table 1: Main characteristics of the study-site.

Figure 1: Picture of the site.

2 Experiment description

2.1 Ambient Vibrations

The ground surface is permanently subjected to ambient vibrations due to:

- natural sources (ocean and large-scale atmospheric phenomena) below $1\,Hz$,

- local meteorological conditions (wind and rain) at frequencies around $1\,Hz$,

- human activities (industrial machines, traffic...) at frequencies above $1\,Hz$ [Bonnefoy-Claudet et al., 2006].

The objective of the measurements is to record these ambient vibrations and to use their propagation properties to infer the underground structure. First, the polarization of the recorded waves (H/V ratio) is used to derive the resonance frequencies of the soil column. Second, the arrival time delays at many different stations are used to derive the velocity of surface waves at different frequencies (dispersion). The information (H/V, dispersion curves) is then used to derive the properties of the soil column using an inversion process.

2.2 Equipment

For the single station measurement campaign, 1 Quanterra Q330 logger and 1 Lennartz 3C 5s seismometer was used. The sensor were set directly on the ground, time stamping was based on the station internal clock.

For the array measurements, 12 Quanterra Q330 dataloggers named NR01 to NR12 and 14 Lennartz 3C 5 s seismometers were available (see Tab. 2). Each datalogger can record on 2 ports A (channels EH1, EH2, EH3 for Z, N, E directions) and B (channels EH4, EH5, EH6 for Z, N, E directions). Time synchronization was ensured by GPS. The sensors were placed on a metal tripod in a $20\,cm$ deep hole, when possible, for better coupling with the ground.

Digitizer	Model	Number	Resolution
	Quanterra Q330	1	24 bits
	Quanterra Q330	12	24 bits
Sensor type	**Model**	**Number**	**Cut-off frequency**
Velocimeter	Lennartz 3C	1	0.2 Hz
Velocimeter	Lennartz 3C	14	0.2 Hz

Table 2: Equipment used.

2.3 Location of the measurements

A grid of 10 points was performed in the city of Interlaken to perform single station measurements (see map on Fig. 2). In addition, 3 test stations (1 week recordings) were installed but are not described further in this report.

In addition, two arrays were performed. The first array (large) was performed in the Höhe-matte field, a large open space in the city centre, with 3 rings (14 points) of 50, 100 and 225 m radius around a central station, with 5 sensors per ring except the largest one (3 stations). The minimum inter-station distance and the aperture are therefore 50 and 450 m. The second array (small) was performed close to the castle where station SINS is installed, with a centre 200 m away from the first array. It consists in 3 rings (14 points) of 10, 20 and 40 m radius around a central station. The minimum inter-station distance and the aperture are therefore 10 and 80 m. The experimental setup is displayed in Fig. 3. The final usable datasets are detailed in section 3.2.
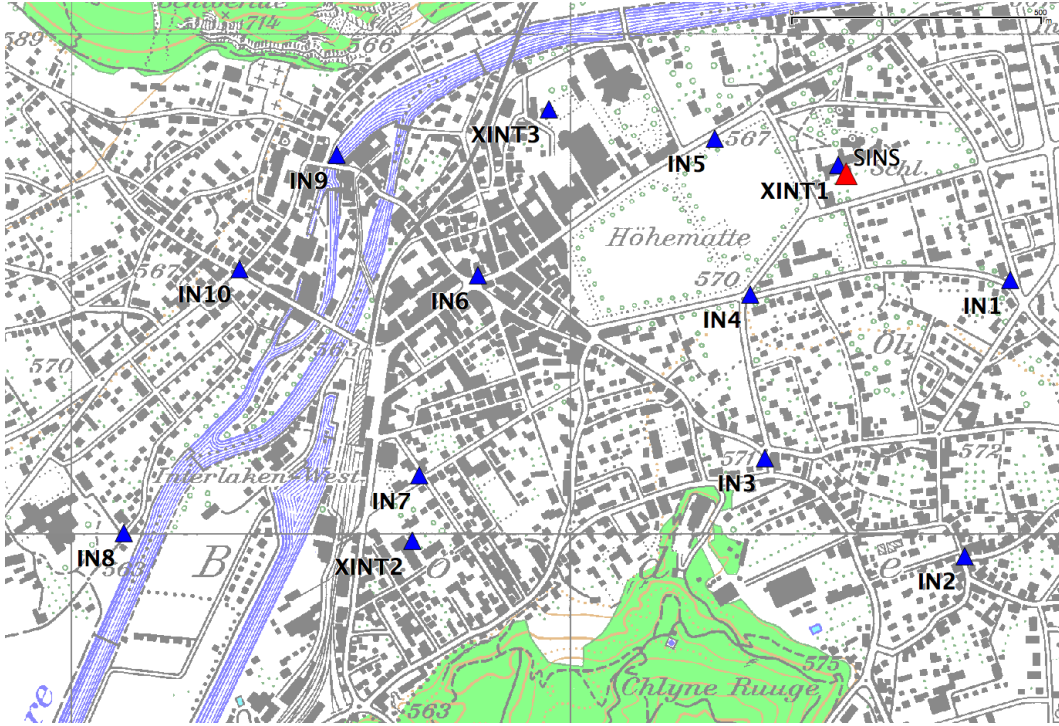

Figure 2: Grid for the single station measurements.

2.4   Positioning of the stations

For the single station measurements, the location of the stations was picked in the 1/25000 map, therefore with an accuracy of several meters.

For the arrays, the sensor coordinates were measured using a differential GPS device (Leica Viva GS10), including only a rover station and using the Real Time Kinematic technique provided by Swisstopo. It allowed an absolute positioning with an accuracy better than 5 cm on the Swissgrid.

Figure 3: Geometry of the arrays; Top: overview of array 1 (large) and 2 (small); Bottom: Zoom on array 2 and station SINS.

3   Data quality

3.1   Usable data

For the single station measurements, the largest time windows were extracted, for which the sensor was installed. No GPS synchronization was used so that the time stamping may be far from the absolute time.

For the array, the largest time windows were extracted, for which all the sensors of the array were correctly placed and the GPS synchronization was ensured. Traffic on the roads around was limited. A light wind was blowing during the measurements. Differential GPS measurements were mostly not performed during the recordings to avoid additional disturbances. Children played close to sensor INT303, which makes it slightly more noisy than the other sensors, together with INT302, which is close to a round-about. Moreover, points 311 and 312, located along the road, are extremely noisy at low frequencies, maybe due to the air flow when cars were passing by. They were not removed for this processing since good results were anyway obtained.

The characteristics of the datasets are detailed in Tab. 3.

3.2   Data processing

The data were first converted to SAC format including header entries for the point coordinates (CH1903 system), the recording component and a name related to the position. For the single station measurement, the name are 2 letters (IN here) and a number from 1 to 10. For the arrays, the name is made of 3 letters characterizing the location (INT here), 1 digit for the ring, 0 or 1 for the first and second array and 1 more digit for the number in the ring. Recordings were not corrected for instrumental response.

Dataset	Starting Date	Time	Length	F_s	Min. inter-distance	Aperture	# of points
IN1	2012/01/26	07:32	36 min	200 Hz			1
IN2	2012/01/26	08:25	31 min	200 Hz			1
IN3	2012/01/26	09:18	33 min	200 Hz			1
IN4	2012/01/26	10:08	32 min	200 Hz			1
IN5	2012/01/26	11:02	31 min	200 Hz			1
IN6	2012/01/26	11:55	31 min	200 Hz			1
IN7	2012/01/26	12:46	33 min	200 Hz			1
IN8	2012/01/26	13:39	34 min	200 Hz			1
IN9	2012/01/26	14:34	32 min	200 Hz			1
IN10	2012/01/26	15:30	32 min	200 Hz			1
1	2012/08/21	9:42	122 min	200 Hz	50 m	450 m	14
2	2012/08/21	14:36	92 min	200 Hz	10 m	80 m	14

Table 3: Usable datasets.

4 H/V processing

4.1 Processing method and parameters

In order to process the H/V spectral ratios, several codes and methods were used. The classical H/V method was applied using the Geopsy http://www.geopsy.org software. In this method, the ratio of the smoothed Fourier Transform of selected time windows are averaged. Tukey windows (cosine taper of 5% width) of $50\,\mathrm{s}$ long overlapping by 50% were selected. Konno and Ohmachi [1998] smoothing procedure was used with a b value of 60. The classical method computed using the method of Fäh et al. [2001] was also performed.

Moreover, the time-frequency analysis method [Fäh et al., 2009] was used to estimate the ellipticity function more accurately using the Matlab code of V. Poggi. In this method, the time-frequency analysis using the Wavelet transform is computed for each component. For each frequency, the maxima over time (10 per minute with at least $0.1\,\mathrm{s}$ between each) in the TFA are determined. The Horizontal to Vertical ratio of amplitudes for each maximum is then computed and statistical properties for each frequency are derived. A Cosine wavelet with parameter 9 is used. The mean of the distribution for each frequency is stored. For the sake of comparison, the time-frequency analysis of Fäh et al. [2001], based on the spectrogram, was also used, as well as the wavelet-based TFA coded in Geopsy.

Method	Freq. band	Win. length	Anti-trig.	Overlap	Smoothing
Standard H/V Geopsy	$0.2-20\,\mathrm{Hz}$	$50\,\mathrm{s}$	No	50%	K&O 60
Standard H/V D. Fäh	$0.2-20\,\mathrm{Hz}$	$30\,\mathrm{s}$	No	75%	-
H/V TFA Geopsy	$0.2-20\,\mathrm{Hz}$	Morlet m=8 fi=1	No	-	-
H/V TFA D. Fäh	$0.2-20\,\mathrm{Hz}$	Specgram	No	-	-
H/V TFA V. Poggi	$0.2-20\,\mathrm{Hz}$	Cosine wpar=9	No	-	No

Table 4: Methods and parameters used for the H/V processing.

4.2 Results in the arrays

The results are coherent in the arrays with a clear fundamental peak at $0.51\,\mathrm{Hz}$ for both arrays with the exception of INT311 and INT312, which were disturbed by the road as explained above (Fig. 4). The fundamental frequency at the SINS station is therefore $0.51\,\mathrm{Hz}$, with a high peak amplitude of 8.

Moreover, all the methods to compute H/V ratios are compared at the array centre on Fig. 5, in which the classical methods were divided by $\sqrt{2}$ to correct from the Love wave contribution [Fäh et al., 2001]. The classical, TFA and FK Capon methods match well.

4.3 Results in the Interlaken city

The single station measurements performed in the city (Fig. 6 and Fig. 7) show that the site of the SINS station is the part of the basin with the lowest frequencies, even if data is lacking to
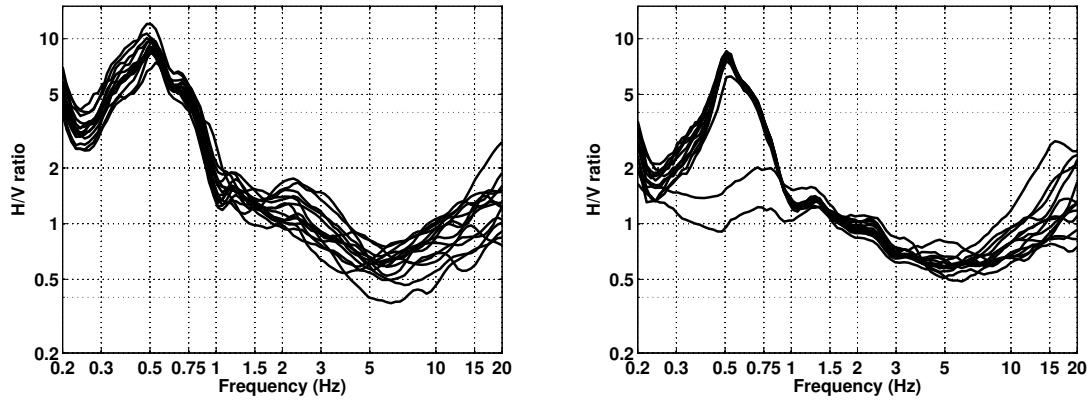
Figure 4: H/V spectral ratios (time-frequency analysis code V. Poggi) of array 1 (left) and 2 (right).
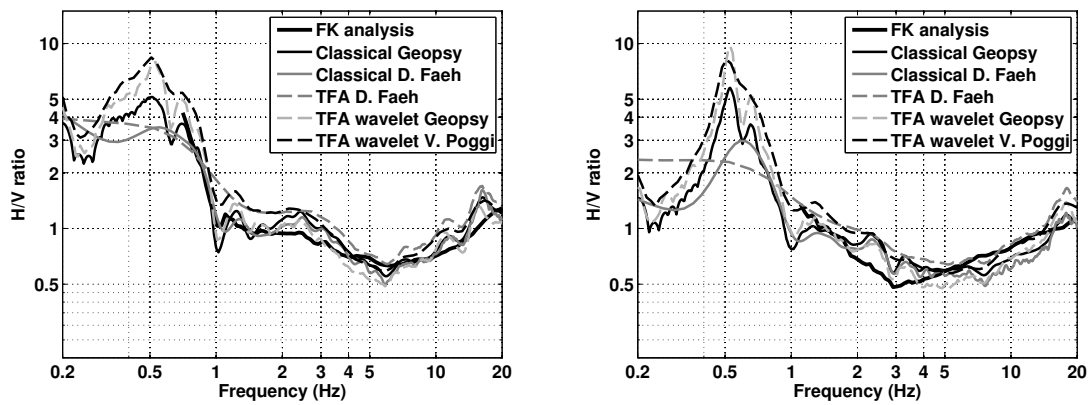

Figure 5: H/V spectral ratios for point INT000 (left) and INT010 (right) using the different codes. Classical methods were divided by $\sqrt{2}$.

fully map the frequencies especially towards East. The frequency is increasing towards West and close to the edges. In the city centre, the frequency is $0.6\,\mathrm{Hz}$ so not very different from the SINS station, so that this station is representative for the Interlaken city.
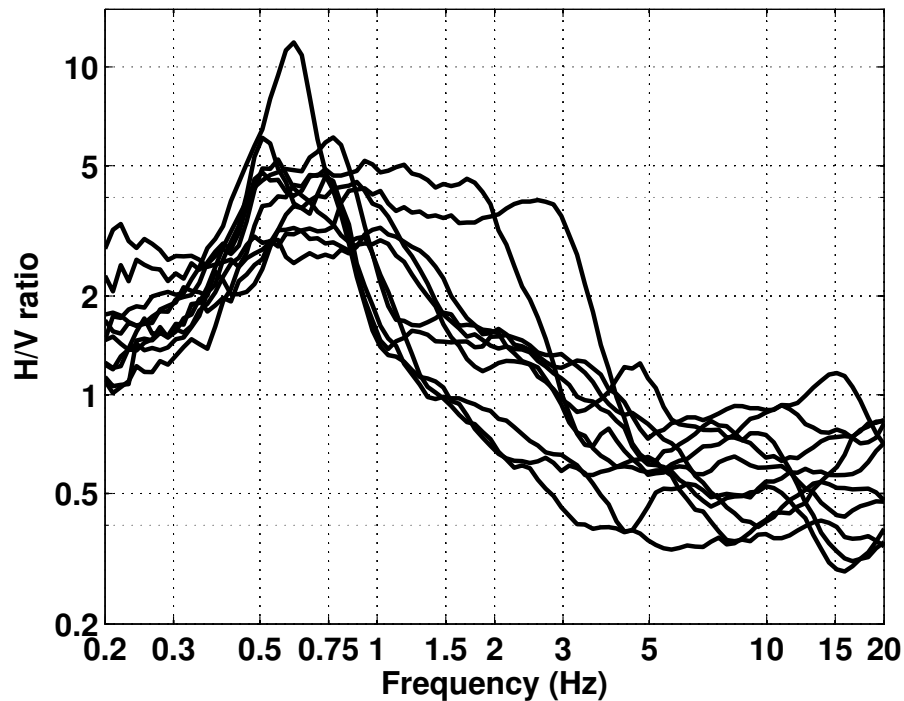

Figure 6: H/V spectral ratios for the single station measurements in Interlaken (time-frequency analysis code V. Poggi).

4.4 Polarization analysis

Since the frequency $0.51\,\mathrm{Hz}$ was found on a large area, a polarization analysis using the code of Burjánek et al. [2010] was performed in order to determine if it is related to 2D resonance. The results show clearly a polarization at this frequency in the direction approximately E-W, corresponding to the valley axis between the two lakes, for all sensors of array 1 (Fig. 8). This resonance corresponds therefore to a 2D resonance and the ellipticity information is therefore not used in the 1D inversion.
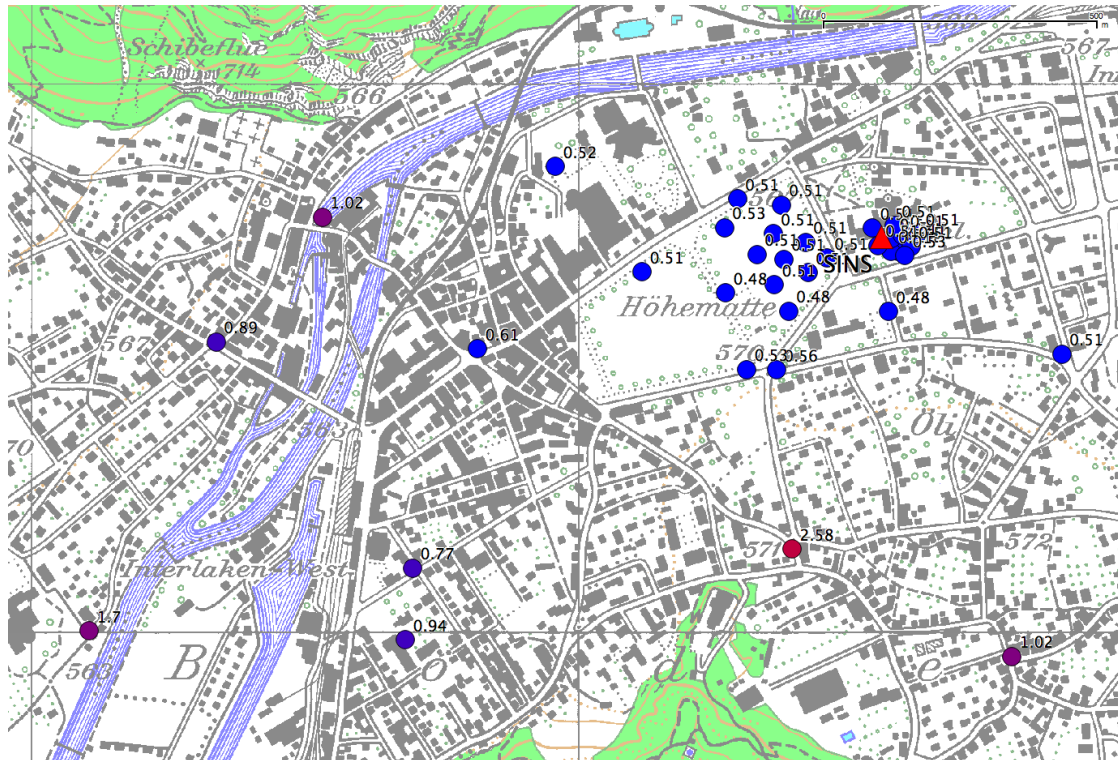
Figure 7: Map of the fundamental resonance frequencies (Hz) in Interlaken (code V. Poggi).
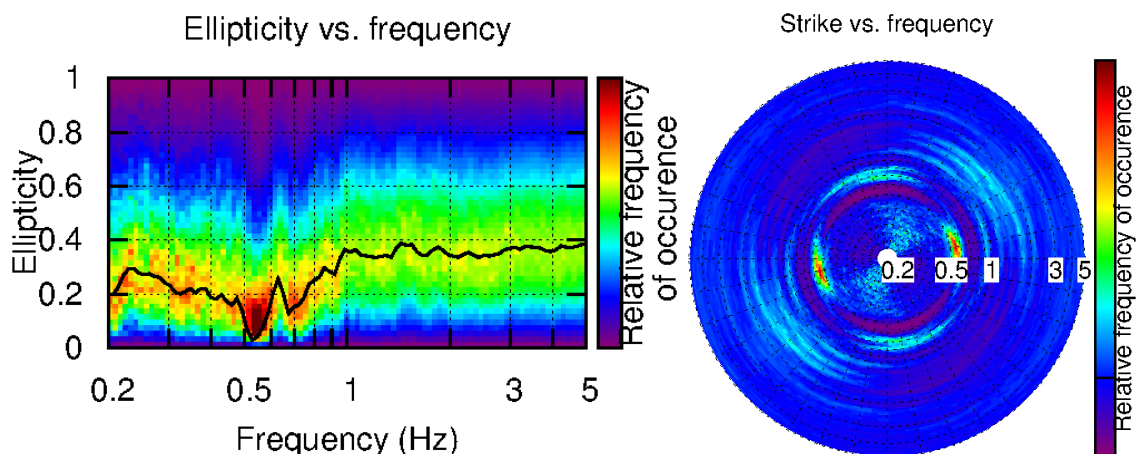

Figure 8: Polarization analysis at point INT000. Left: Ellipticity (A trough in the ellipticity corresponds to polarized motion). Right: Strike of the polarization.

5 Array processing

5.1 Processing methods and parameters

The vertical components of the arrays were processed using the High-resolution FK analysis [Capon, 1969] using the Geopsy `http://www.geopsy.org` software. Better results were obtained using large time windows (300T). Dispersion curves were picked separately for each dataset.

Moreover, a 3C array analysis [Fäh et al., 2008] was also performed using the 3C_array_analysis software [Poggi and Fäh, 2010]. It allows to derive Rayleigh and Love modes including the Rayleigh ellipticity. Dispersion curves were picked separately for each dataset.

Method	Set	Freq. band	Win. length	Anti-trig.	Overlap	Grid step	Grid size	# max.
HRFK 1C	1	$0.4 - 25\,\text{Hz}$	$300T$	No	50%	0.001	0.8	5
HRFK 1C	2	$0.4 - 25\,\text{Hz}$	$300T$	No	50%	0.001	0.8	5
HRFK 3C	1	$0.4 - 22\,\text{Hz}$	Wav. 10 Tap. 0.2	No	50%	150 m/s	2000 m/s	5
HRFK 3C	2	$0.4 - 22\,\text{Hz}$	Wav. 10 Tap. 0.2	No	50%	150 m/s	2000 m/s	5

Table 5: Methods and parameters used for the array processing.

5.2 Obtained dispersion curves

The first mode (Rayleigh) in the 1C FK analysis could be picked between 1 and $7.4\,\text{Hz}$ and 1 and $21\,\text{Hz}$ (Fig. 9) for the first and second datasets, respectively, including its standard deviation. The phase velocities are ranging from $1000\,\text{m/s}$ at $1\,\text{Hz}$ down to $250\,\text{m/s}$ at $21\,\text{Hz}$.

Using the 3C analysis, both fundamental Rayleigh and Love modes can be picked, as well as the first higher Love mode (Fig. 10). Some discrepancies are noticed with the 1C analysis. Finally, Rayleigh fundamental mode can be picked between 1 and $22\,\text{Hz}$ with a high confidence (Fig. 11). Love modes are slightly more complicated. Using dataset 1, the fundamental mode can be accurately picked between 0.8 and $4\,\text{Hz}$ (Fig. 11). However, all the other picked parts seem to belong to the first higher mode, that is finally found from 2.3 to $17.3\,\text{Hz}$ (Fig. 11). It is interesting to see that the fundamental Love mode cannot be seen at all on the dataset 2. For the inversion, the Rayleigh mode was cut at $13\,\text{Hz}$ because there may be a mode osculation at this frequency (curve going up) or a velocity inversion but there is too few information to conclude.

Finally, even though the arrays do not have the same centre, their dispersion curves are fully compatible so that broad band curves could be derived. It also shows that the lateral variability is low in this area. The ellipticity curves from the 3C analysis, on the contrary, are not exactly the same, which may be due to different array resolution limits.
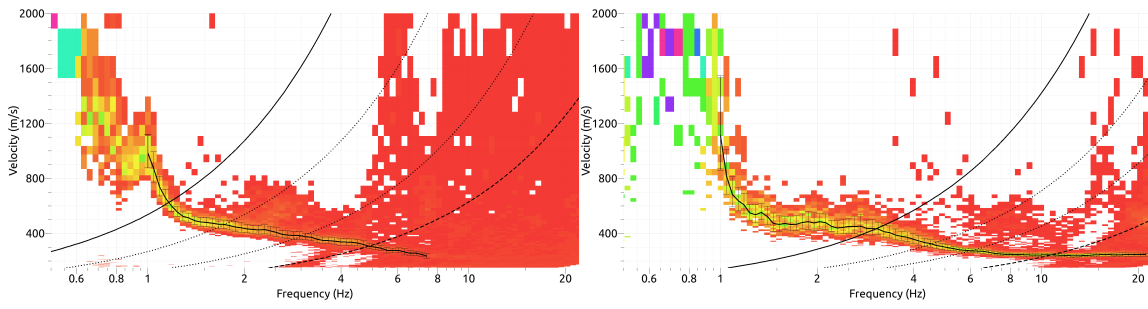
Figure 9: Dispersion curves obtained from the 1C array analysis (left: dataset 1, right: dataset 2).
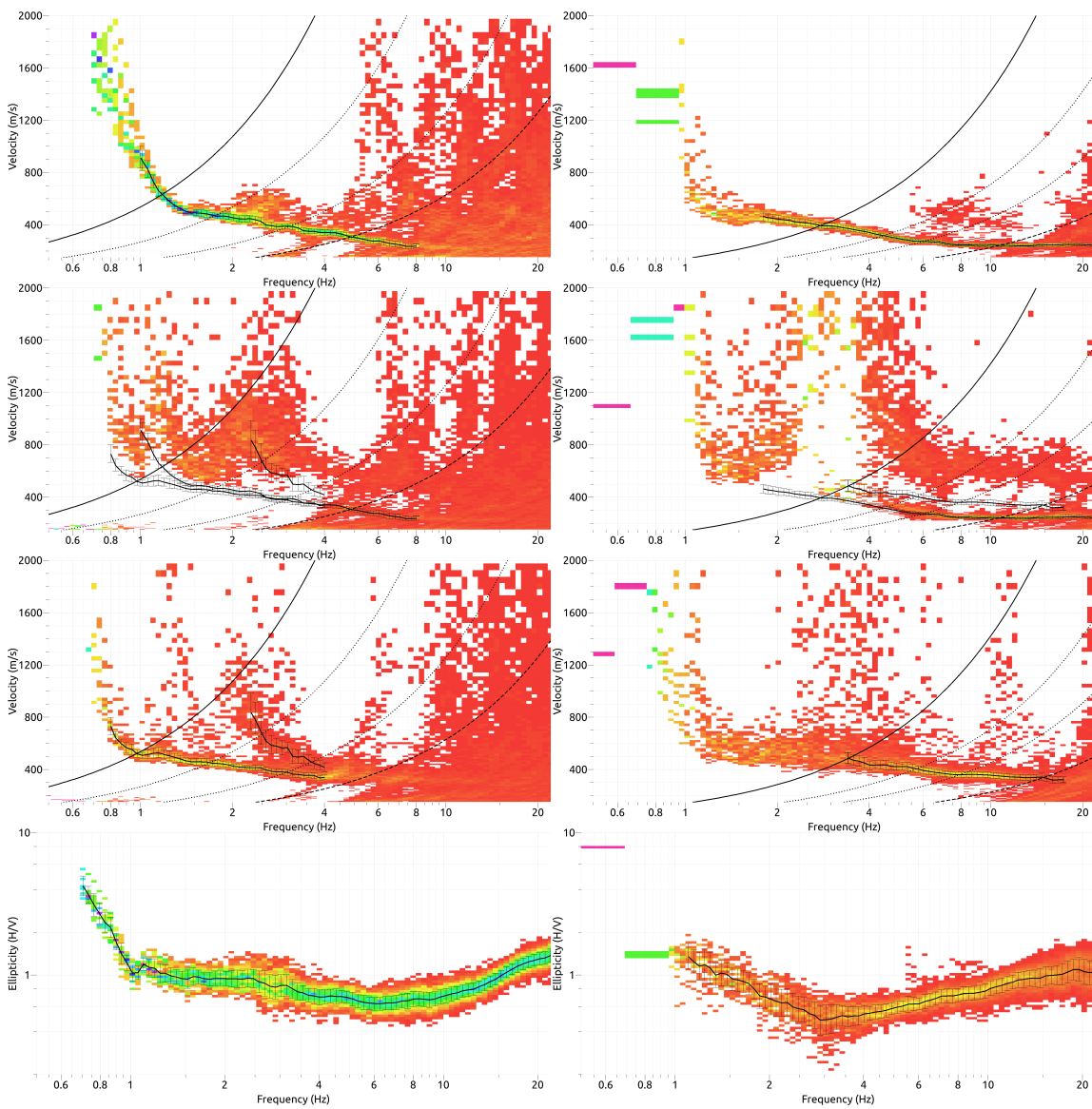

Figure 10: Dispersion curves and ellipticity obtained from the 3C array analysis (from top to bottom: vertical, radial, transverse and ellipticity; left: dataset 1, right: dataset 2).
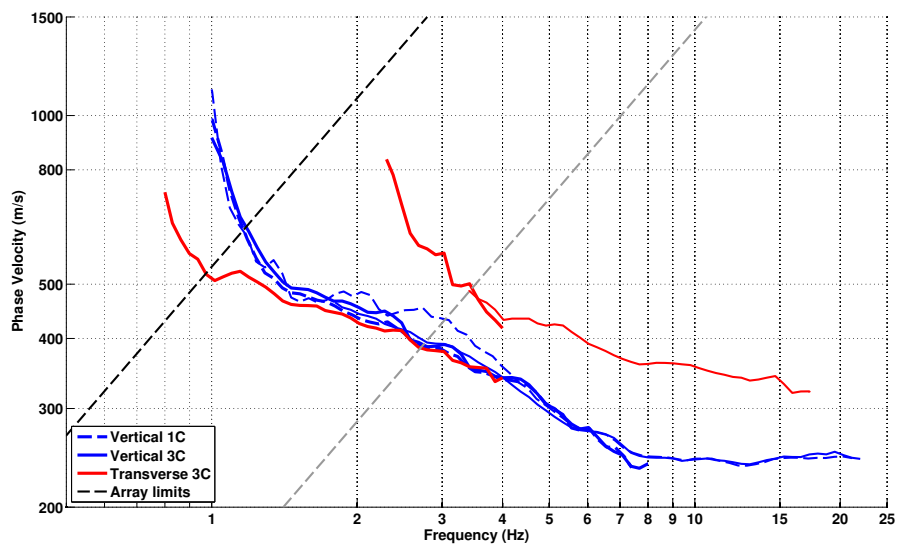
Figure 11: Picked Rayleigh (blue) and Love (red) dispersion curves from 1C (dashed lines) and 3C (solid lines) methods from dataset 1 (thick lines) and 2 (thin lines).

6   Inversion and interpretation

6.1   Inversion

For the inversion, Rayleigh and Love fundamental modes and Love first higher mode dispersion curves were used as simultaneous targets without standard deviation to avoid different weighting. Due to the 2D resonance, the ellipticity information is not used, though the ellipticity curve is displayed for comparison in the following. The results from the 3C FK analysis were used. All curves were resampled using 50 points between 0.4 and $23\,\mathrm{Hz}$ in log scale.

The inversion was performed using the Improved Neighborhood Algorithm (NA) [Wathelet, 2008] implemented in the Dinver software. In this algorithm, the tuning parameters are the following: Ns_0 is the number of starting models, randomly distributed in the parameter space, Nr is the the number of best cells considered around these Ns_0 models, Ns is the number of new cells generated in the neighborhood of the Nr cells (Ns/Nr per cell) and It_{max} is the number of iteration of this process. The process ends with $Ns_0 + Nr * \frac{Ns}{Nr} * It_{max}$ models. The used parameters are detailed in Tab. 6.

It_{max}	Ns_0	Ns	Nr
500	10000	100	100

Table 6: Tuning parameters of Neighborhood Algorithm.

During the inversion process, low velocity zones were not allowed. The Poisson ratio was inverted in each layer in the range 0.2-0.4, up to 0.47 just below the assumed water table. The density was supposed equal to $2000\,\mathrm{kg/m}^3$ except for the deepest layers ($2500\,\mathrm{kg/m}^3$). Inversions with free layer depths as well as fixed layer depths were performed. Since the dispersion curves were not constraining the bedrock properties, they were assumed in the inversion. Assuming the topographic slope of the rock surrounding the valley remains constant below the sediments ($42\,°$ from the Swisstopo map), the sediment thickness is found to be around $380\,\mathrm{m}$ below the SINS station. This value is confirmed in the next section. The bedrock is therefore fixed at this depth with $V_s = 2500\,\mathrm{m/s}$. 5 layers are enough to explain most of the targets (dispersion curves), but more layers are used to smooth the obtained results and better explore the parameter space. 5 independent runs of 5 different parametrization schemes (6 and 7 layers over a half space and 12, 15 and 18 layers with fixed depth) were performed. For further elaborations, the best models of these 25 runs were selected (Fig. 15).

Below the first 3 meters that show low velocity values, a first layer down to $30\,\mathrm{m}$ depth with relatively homogeneous velocity ($300\,\mathrm{m/s}$) is found. At this depth, a clear interface is found. Below, the velocity is around $450\,\mathrm{m/s}$. This velocity is constant down to 130 to $150\,\mathrm{m}$ depth, where it increases up to $750\,\mathrm{m/s}$ in a layer that is found down to the bedrock with slightly increasing velocity. This last part, however, is not much constrained by the data.
Boreholes in the surroundings were found in the geoportal of canton Bern (under `http://www.map.apps.be.ch/pub/synserver`) but no borehole deeper than $20\,\mathrm{m}$ was found in this zone.

When comparing to the target curves (Fig. 13 and Fig. 14), all curves are well represented. The ellipticity curve, that is not inverted, matches the H/V curve.
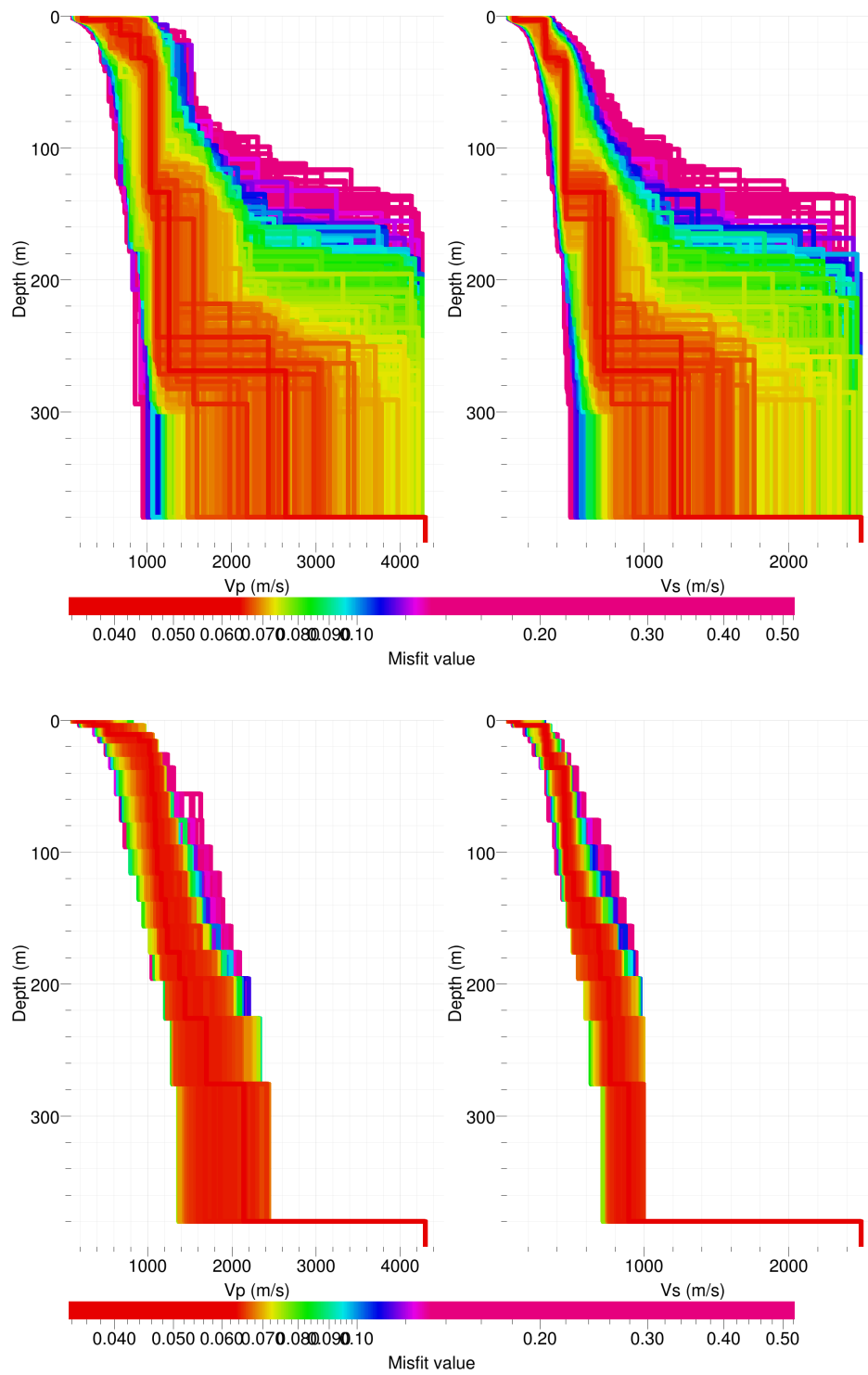
Figure 12: Inverted ground profiles in terms of V_p and V_s; top: free layer depth strategy; bottom: fixed layer depth strategy.
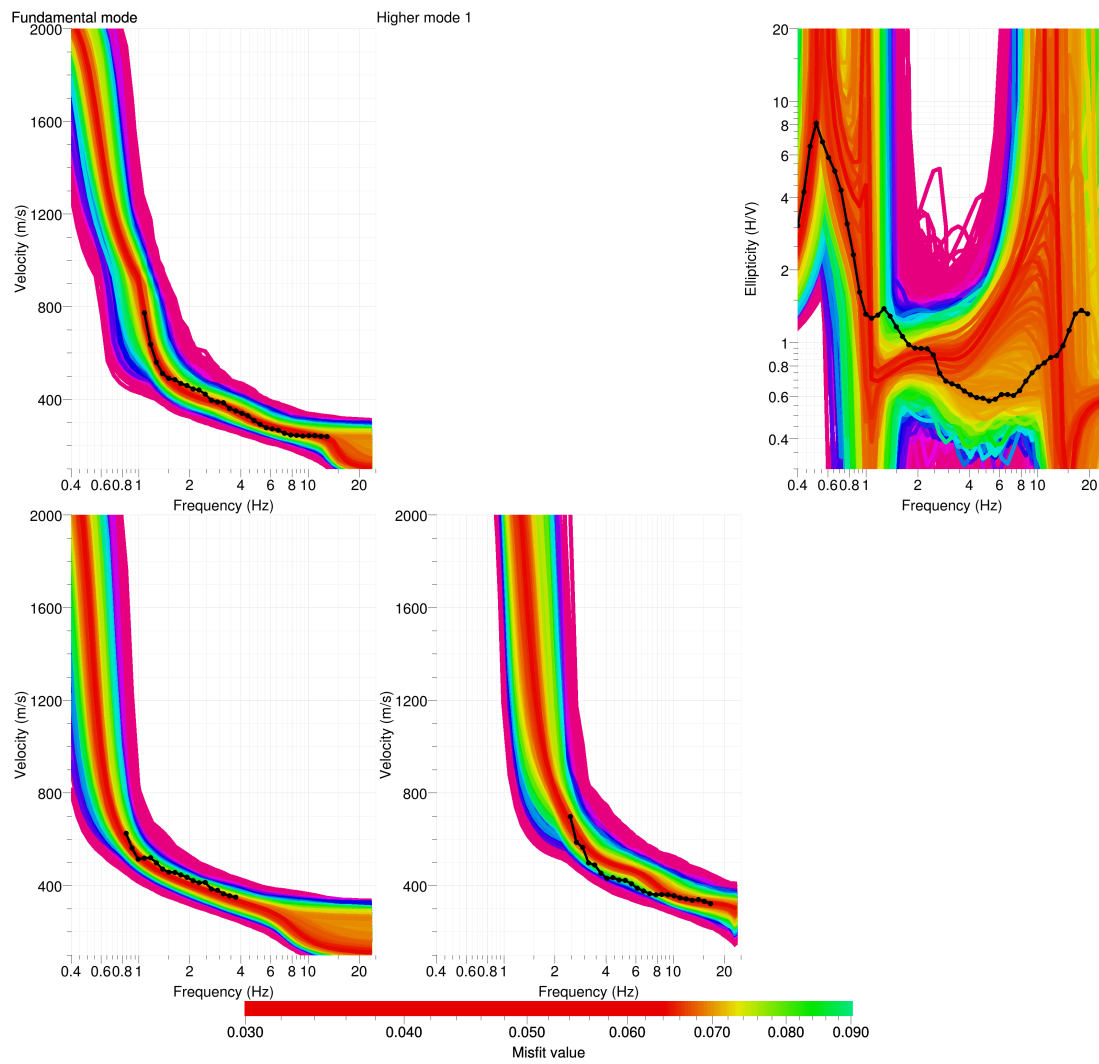
Figure 13: Comparison between inverted models and measured Rayleigh and Love modes and corresponding ellipticity, free layer depth strategy.
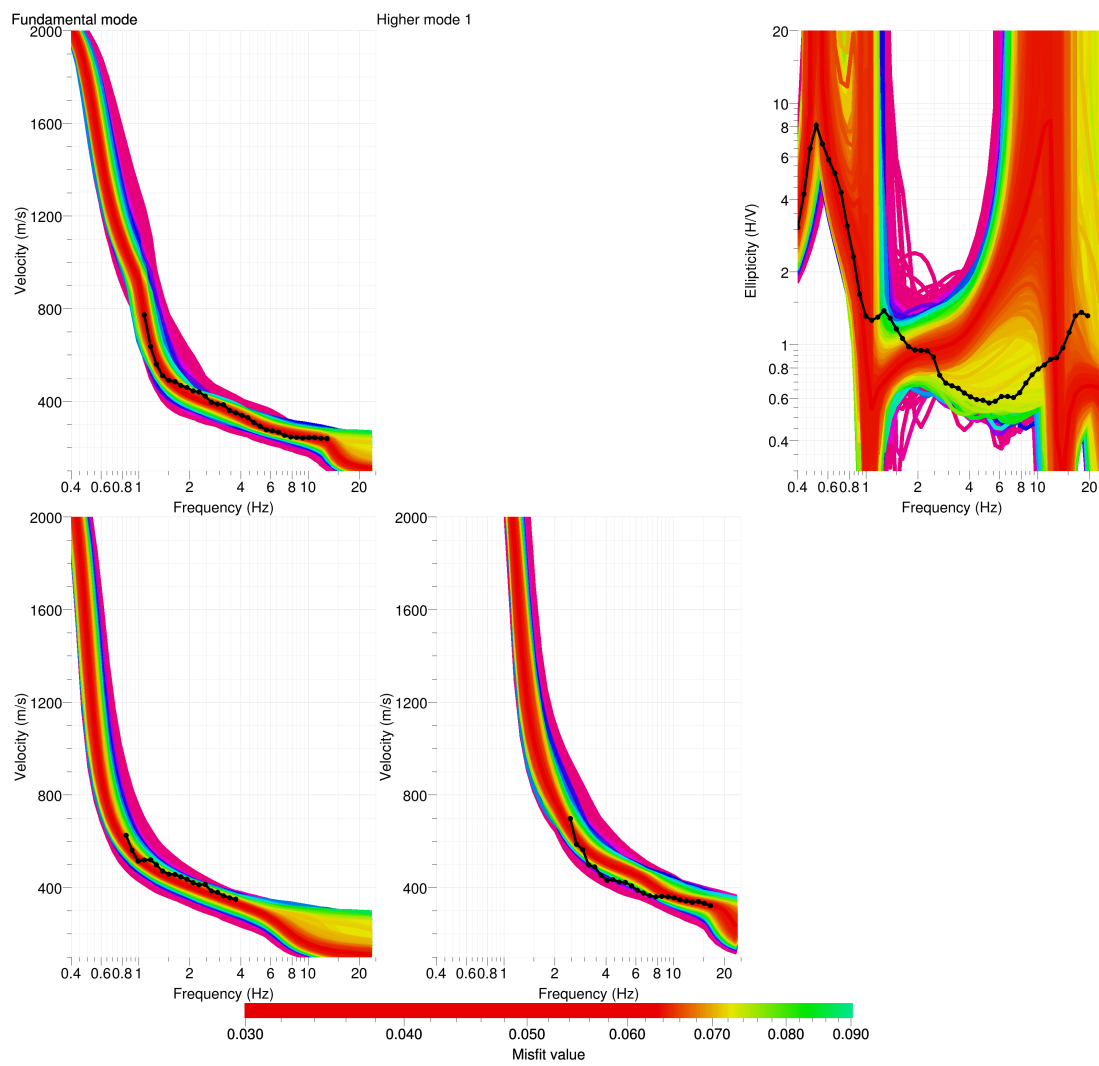
Figure 14: Comparison between inverted models and measured Rayleigh and Love modes and corresponding ellipticity, fixed layer depth strategy.
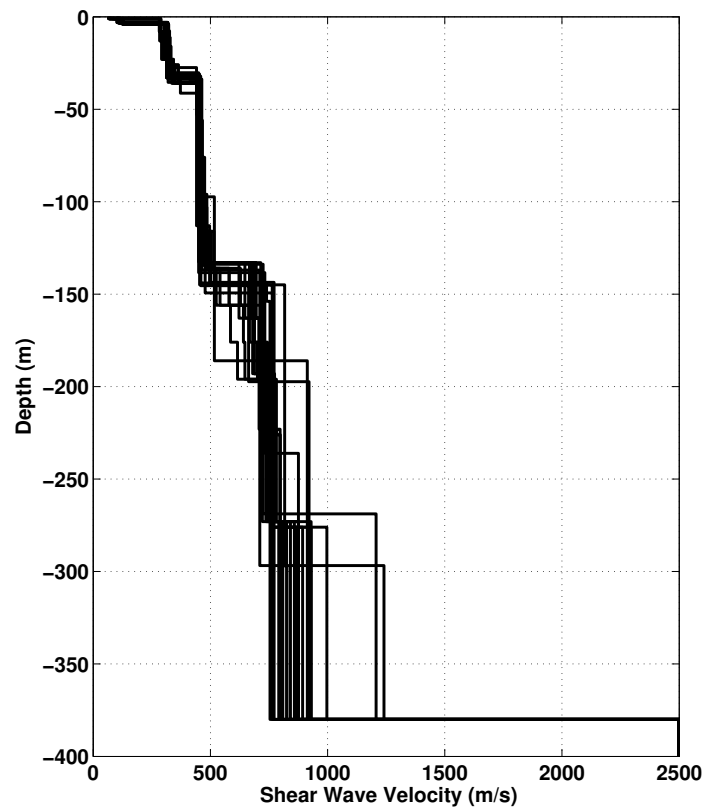
Figure 15: V_s ground profiles for the selected 25 best models.

6.2   Travel time average velocities and ground type

The distribution of the travel time average velocities at different depths was computed from the selected models. The uncertainty, computed as the standard deviation of the distribution of travel time average velocities for the considered models, is also provided, but its meaning is doubtful. $V_{s,30}$ is found to be $266\,\mathrm{m/s}$, which corresponds to class C in the Eurocode 8 [CEN, 2004] and class D in SIA261 [SIA, 2003].

	Mean (m/s)	Uncertainty (m/s)
$V_{s,5}$	152	21
$V_{s,10}$	202	15
$V_{s,20}$	245	8
$V_{s,30}$	266	5
$V_{s,40}$	291	5
$V_{s,50}$	313	5
$V_{s,100}$	371	3
$V_{s,150}$	407	5
$V_{s,200}$	455	6

Table 7: Travel time averages at different depths from the inverted models. Uncertainty is given as one standard deviation from the selected profiles.

6.3   SH transfer function and quarter-wavelength velocity

The quarter-wavelength velocity approach [Joyner et al., 1981] provides, for a given frequency, the average velocity at a depth corresponding to 1/4 of the wavelength of interest. It is useful to identify the frequency limits of the experimental data (minimum frequency in dispersion curves at $0.85\,\mathrm{Hz}$ here). The results using this proxy show that the dispersions curves constrain the profiles down to $115\,\mathrm{m}$ (Fig. 16). Moreover, the quarter wavelength impedance-contrast introduced by Poggi et al. [2012] is also displayed in the figure. It corresponds to the ratio between two quarter-wavelength average velocities, respectively from the top and the bottom part of the velocity profile, at a given frequency [Poggi et al., 2012]. It shows a trough (inverse shows a peak) at the resonance frequency (too low for this figure).

Moreover, the theoretical SH-wave transfer function for vertical propagation [Roesset, 1970] is computed from the inverted profiles. It is compared to the quarter-wavelength amplification [Joyner et al., 1981], that however cannot take resonances into account (Fig. 17). In this case, the models are predicting an amplification up to a factor of 6 at the resonance frequencies and their harmonics, especially at $2\,\mathrm{Hz}$. Since the behaviour is 2D and the information at depth is sparse, these models are however very uncertain.
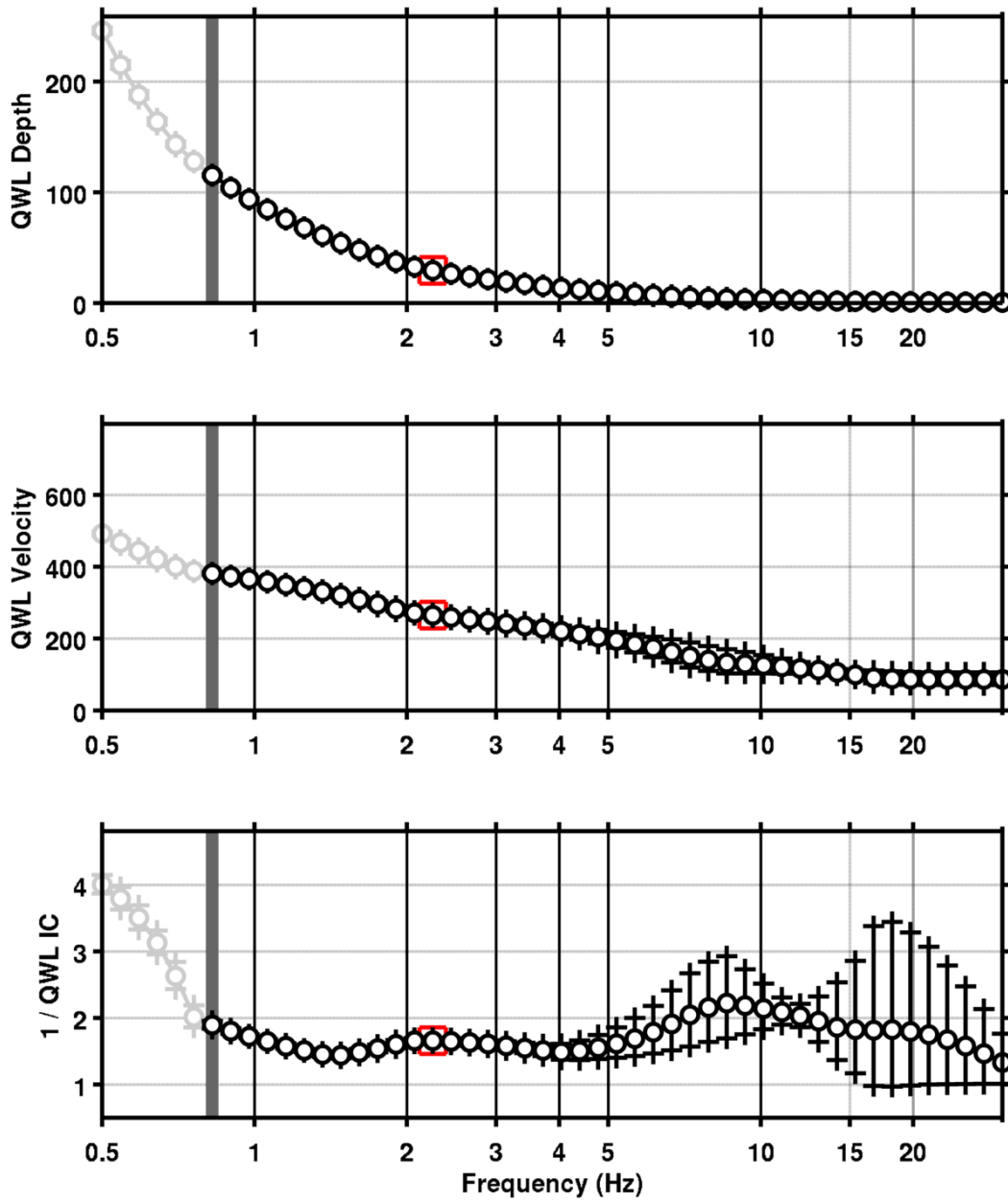
Figure 16: Quarter wavelength velocity representation of the velocity profile (top: depth, centre: velocity, bottom: inverse of the impedance contrast). Black curve is constrained by the dispersion curves, light grey is not constrained by the data. Red square is corresponding to $V_{s,30}$.
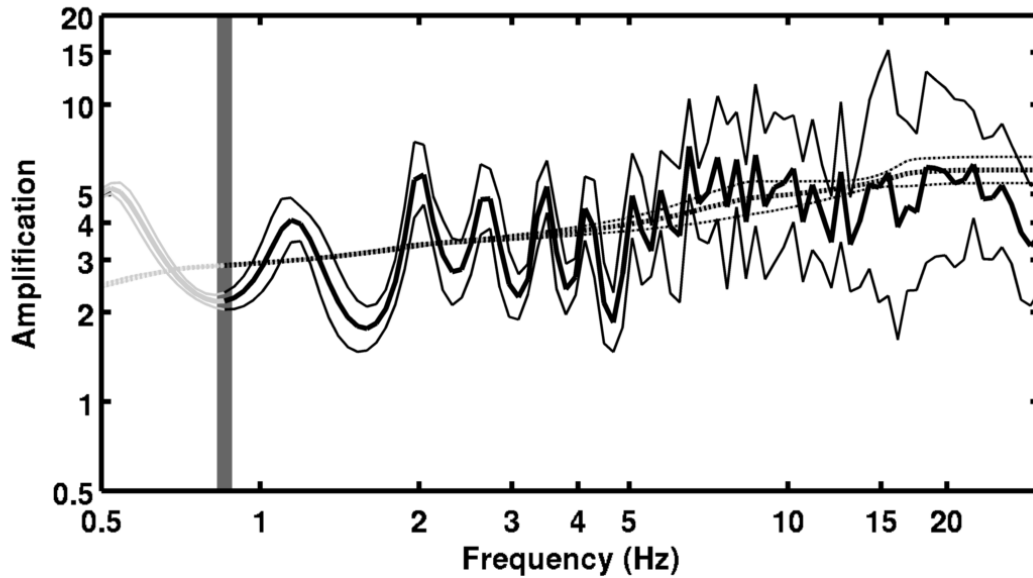
Figure 17: Theoretical SH transfer function (solid line) and quarter wavelength impedance contrast (dashed line) with their standard deviation. Significance of the greyshades is detailed in Fig. 16.

7 2D resonance

Since the polarization analysis showed that the Interlaken basin had a 2D resonance mode, the basin shape and velocity profile was tested against the 2D resonance properties. For this purpose, the code REFORM developed by Paolucci [1999] was used. The cosine valley shape was used with one of the velocity profiles inverted in the previous section (4 layers in the basin). The original idea was to invert for the basin depth H knowing the fundamental SH resonance frequency $f_0 = 0.51$ Hz. However, looking at the map, the last missing parameter, the valley width $2a$, happens to be extremely uncertain (Fig. 18). Indeed, an adjacent valley brought alluvia to the basin at this location eroding and covering geomorphological traces of the basin end in the South. The narrowest valley width is 1200 m and occurs at Interlaken city centre. Conversely, the broadest valley width would be 2500 m assuming that the adjacent valley also participates to this width. The width of the Lake Brienz is 2000 m and an interpolation between the southern side of lake Brienz and the rock outcrop southern of Interlaken city-centre provides a width of 1500 m at the SINS site. Finally, all these values were tested and the depth of the basin H was inverted from the resonance frequency. Using this depth and the cosine shape of the valley and knowing that station SINS is located 400 m South from the basin edge, the bedrock depth at SINS could then be estimated.

For the minimum and maximum values of $2a$, the bedrock depth at SINS is 300 and 1000 m, respectively (Fig. 18). The interpolated value $2a = 1500$ m provides a depth at SINS of 380 m, which is the one extrapolated assuming the slope of the bedrock is constant under the sediments. Finally, this value is the best that can be given with these data, but is still uncertain.

A H/V cross-section of the valley would allow to map more precisely the extension of the basin behaving in a 2D mode.
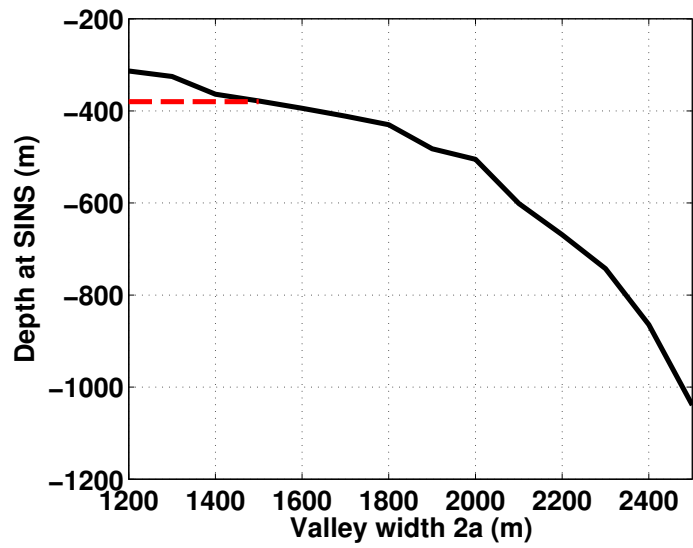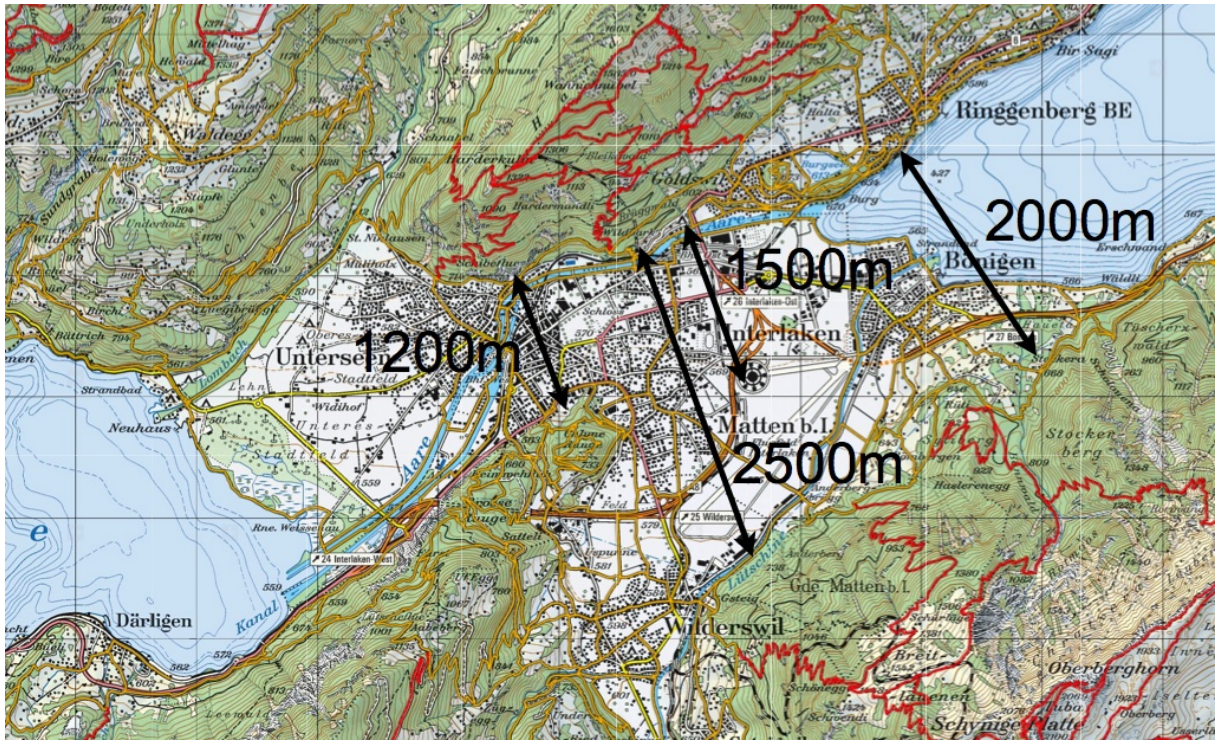
Figure 18: Top: Possible estimates of the valley width in Interlaken; Bottom: Bedrock depth at SINS station for different values of the valley width. In red is the most probable value.

8   Conclusions

The array measurements presented in this study were successful in deriving a velocity model for the site of the SSMNet station SINS in Interlaken. We found, below the first 3 meters that show low velocity values, a first layer down to 30 m depth with relatively homogeneous velocity (300 m/s). At this depth, a clear interface with a layer with a 450 m/s velocity is found down to 130 to 150 m depth. At this depth, it increases up to 750 m/s in a layer that is found down to the bedrock with slightly increasing velocity, at 380 m depth, according to geophysical and geomorphological constraints. The basin is found to be working on a 2D resonance mode, with a fundamental SH frequency of 0.51 Hz.

$V_{s,30}$ is 266 m/s, which corresponds to ground type C in the Eurocode 8 [CEN, 2004] and class D in SIA261 [SIA, 2003]. The theoretical 1D SH transfer function and impedance contrast of the quarter-wavelength velocity computed from the inverted profiles show large amplifications at resonance frequencies over a broad frequency range, but the 2D behavior may have a strong impact on this. Recordings on the new station will allow to compare to these simple models.

Acknowledgements

References

Sylvette Bonnefoy-Claudet, Fabrice Cotton, and Pierre-Yves Bard. The nature of noise wavefield and its applications for site effects studies. *Earth-Science Reviews*, 79(3-4): 205–227, December 2006. ISSN 00128252. doi: 10.1016/j.earscirev.2006.07.004. URL http://linkinghub.elsevier.com/retrieve/pii/S0012825206001012.

Jan Burjánek, Gabriela Gassner-Stamm, Valerio Poggi, Jeffrey R. Moore, and Donat Fäh. Ambient vibration analysis of an unstable mountain slope. *Geophysical Journal International*, 180(2):820–828, February 2010. ISSN 0956540X. doi: 10.1111/j.1365-246X.2009.04451.x. URL http://doi.wiley.com/10.1111/j.1365-246X.2009.04451.x.

J. Capon. High-Resolution Frequency-Wavenumber Spectrum Analysis. *Proceedings of the IEEE*, 57(8):1408–1418, 1969.

CEN. *Eurocode 8: Design of structures for earthquake resistance - Part 1: General rules, seismic actions and rules for buildings*. European Committee for Standardization, en 1998-1: edition, 2004.

Donat Fäh, Fortunat Kind, and Domenico Giardini. A theoretical investigation of average H / V ratios. *Geophysical Journal International*, 145:535–549, 2001.

Donat Fäh, Gabriela Stamm, and Hans-Balder Havenith. Analysis of three-component ambient vibration array measurements. *Geophysical Journal International*, 172(1):199–213, January 2008. ISSN 0956540X. doi: 10.1111/j.1365-246X.2007.03625.x. URL http://doi.wiley.com/10.1111/j.1365-246X.2007.03625.x.

Donat Fäh, Marc Wathelet, Miriam Kristekova, Hans-Balder Havenith, Brigitte Endrun, Gabriela Stamm, Valerio Poggi, Jan Burjanek, and Cécile Cornou. Using Ellipticity Information for Site Characterisation Using Ellipticity Information for Site Characterisation. Technical report, NERIES JRA4 Task B2, 2009.

William B. Joyner, Richard E. Warrick, and Thomas E. Fumal. The effect of Quaternary alluvium on strong ground motion in the Coyote Lake, California, earthquake of 1979. *Bulletin of the Seismological Society of America*, 71(4):1333–1349, 1981.

Katsuaki Konno and Tatsuo Ohmachi. Ground-Motion Characteristics Estimated from Spectral Ratio between Horizontal and Vertical Components of Microtremor. *Bulletin of the Seismological Society of America*, 88(1):228–241, 1998.

Roberto Paolucci. Shear resonance frequencies of alluvial valleys by Rayleigh‚Äôs method. *Earthquake Spectra*, 15(3):503–521, 1999.

Valerio Poggi and Donat Fäh. Estimating Rayleigh wave particle motion from three-component array analysis of ambient vibrations. *Geophysical Journal International*, 180(1):251–267, January 2010. ISSN 0956540X. doi: 10.1111/j.1365-246X.2009.04402.x. URL http://doi.wiley.com/10.1111/j.1365-246X.2009.04402.x.

Valerio Poggi, Benjamin Edwards, and Donat Fäh. Characterizing the Vertical-to-Horizontal Ratio of Ground Motion at Soft Sediment-Sites. *Bulletin of the Seismological Society of America*, 102(6), 2012. doi: 10.1785/0120120039.

J.M. Roesset. Fundamentals of soil amplification. In R. J. Hansen, editor, *Seismic Design for Nuclear Power Plants*, pages 183–244. M.I.T. Press, Cambridge, Mass., 1970. ISBN 978-0-262-08041-5. URL `http://mitpress.mit.edu/catalog/item/default.asp?ttype=2\&tid=5998`.

SIA. *SIA 261 Actions sur les structures porteuses*. Société suisse des ingénieurs et des architectes, Zürich, sia 261:20 edition, 2003.

Marc Wathelet. An improved neighborhood algorithm: Parameter conditions and dynamic scaling. *Geophysical Research Letters*, 35(9):1–5, May 2008. ISSN 0094-8276. doi: 10.1029/2008GL033256. URL `http://www.agu.org/pubs/crossref/2008/2008GL033256.shtml`.

SITE CHARACTERIZATION REPORT
SINS: Interlaken (BE), Schloss

Appendix A - Active seismic

Paolo Bergamo, Clotaire Michel, Walter Imperatori, Donat Fäh

Schweizerischer Erdbebendienst (SED)
Service Sismologique Suisse
Servizio Sismologico Svizzero
Servizi da Terratrembels Svizzer

ETH Zurich
Sonnegstrasse 5
8092 Zuerich
Schweiz
paolo.bergamo@sed.ethz.ch

A1 Active seismic measurements

Although station SINS had already been characterized during the first phase of the SSMNET renewal project (Michel et al., 2013), the site was selected for further investigations to assess the potential for soil liquefaction triggered by earthquakes. Due to its widespread use in evaluating the likelihood of liquefaction phenomena (Robertson 2004), a CPT test (cone penetration test) was carried out in close proximity to station SINS (Figure A1) on 10.03.2017.

In general, CPT tests are usually conducted in parallel with a downhole seismic survey, performed by placing one or two geophones close to the CPT probe (the two coupled tests are called SCPT, or seismic CPT: Robertson et al., 1986). As the conical probe is driven deeper and deeper into the subsurface, its progression is stopped at regular intervals (e.g. 1 m) and a seismic source signal is generated at the surface. The propagation of generated P- and S-waves is recorded by the geophone(s) at depth, so that a V_P and V_S profile for the investigated subsurface can be reconstructed. SCPT tests provide a comprehensive characterization of the subsoil in terms of both stratigraphic strength and modulus information.

However, due to logistical reasons, in the case of station SINS only the CPT measurement could be carried out. To provide a detailed V_S model of the shallow subsurface (first 30 m, expected depth of CPT survey), a non-invasive active seismic test was performed on 3.03.2017 close to SINS station and to the CPT location (Figure A1).

For the sake of a comprehensive subsurface characterization, multichannel analysis of surface waves (MASW; Park et al., 1999) and P-wave refraction (Redpath, 1973) surveys were conducted.

A1.1 Equipment and geometry of the acquisition array

We used two sets of 24 vertical-component geophones (30 Hz corner frequency). Each geophone set was connected to a Geode datalogger; the two Geodes were coupled for time synchronization. The seismic source was a 5-kg sledgehammer, hitting a flat metal plate.

The 48 receivers were aligned at regular intervals of 1 m, for a total length of the array line of 47 m. The geophones were laid on agricultural soil, with metal spikes ensuring a firm coupling with the ground (Figure A2).

As earlier anticipated, MASW and P-wave refraction measurements were performed. As for refraction surveys, the source was placed at four locations along the receivers' line: at both ends, and at 1/3 and 2/3 of the spread (src2-5, Figure A1). Two additional MASW shooting positions were placed at both edges of the line, 10 m away from the closest geophone (src1,6 Figure A1).
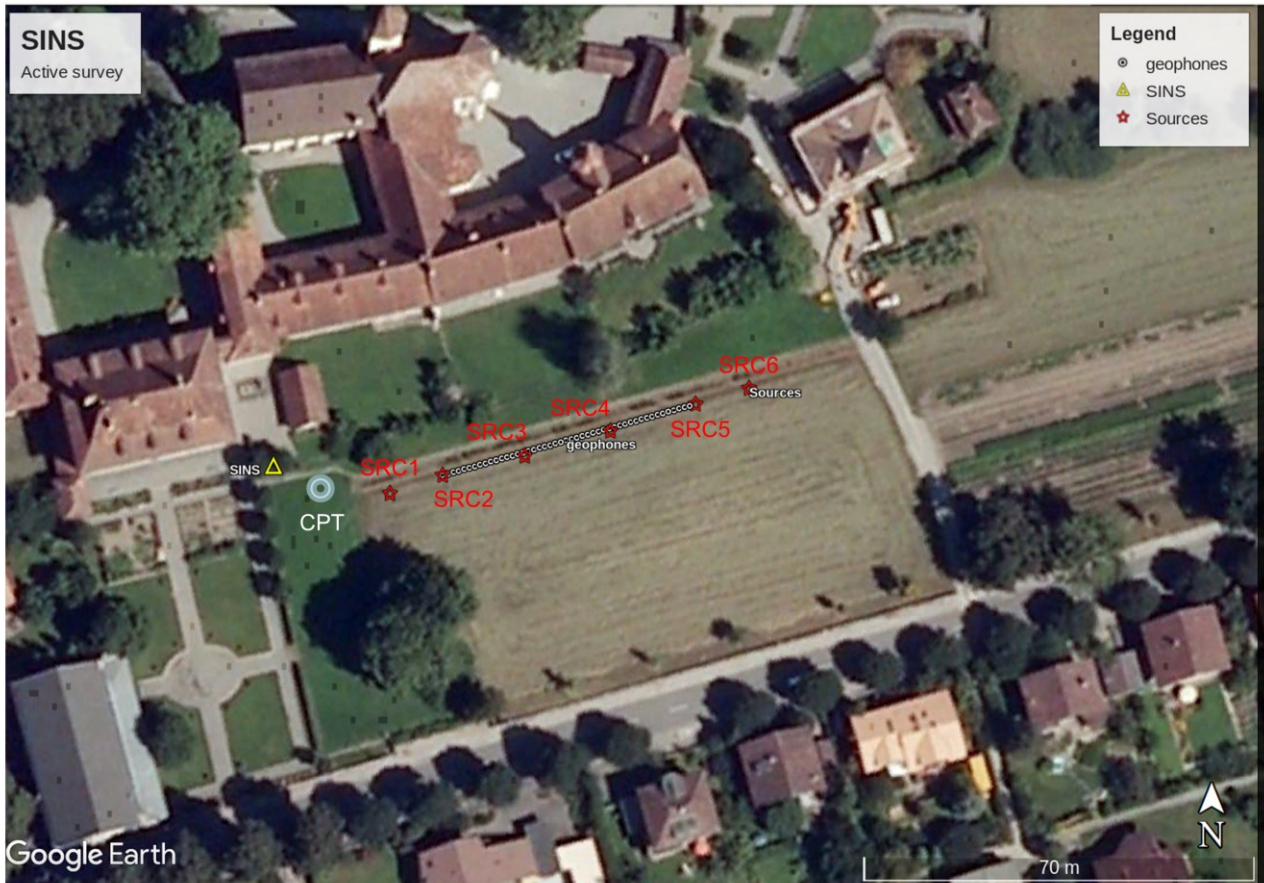
Figure A1 – Map representing the position of the targeted station (SINS), of the active seismic line and of the CPT survey (© 2016 GoogleMaps).

Figure A2 – Seismic array in place.

A1.2 Acquisition

The time-sampling parameters adopted for both MASW and refraction acquisitions were the following: sampling interval = 62.5 µs, record length = 2 s, pre-trigger delay = -0.1 s. At each source point (src1-6), 10 hammer blows were successively shot: for each hammer blow, the traces recorded by all geophones were saved in a separate *.sg2* file.

In Figure A3a, a sample single-shot seismic section acquired having positioned the source in src1 is represented. The data quality is generally good, the propagation of the hammer-blow signal is clear; however, at long offset (> 50 m, last 6-7 traces) the effect of undesired noise is evident.
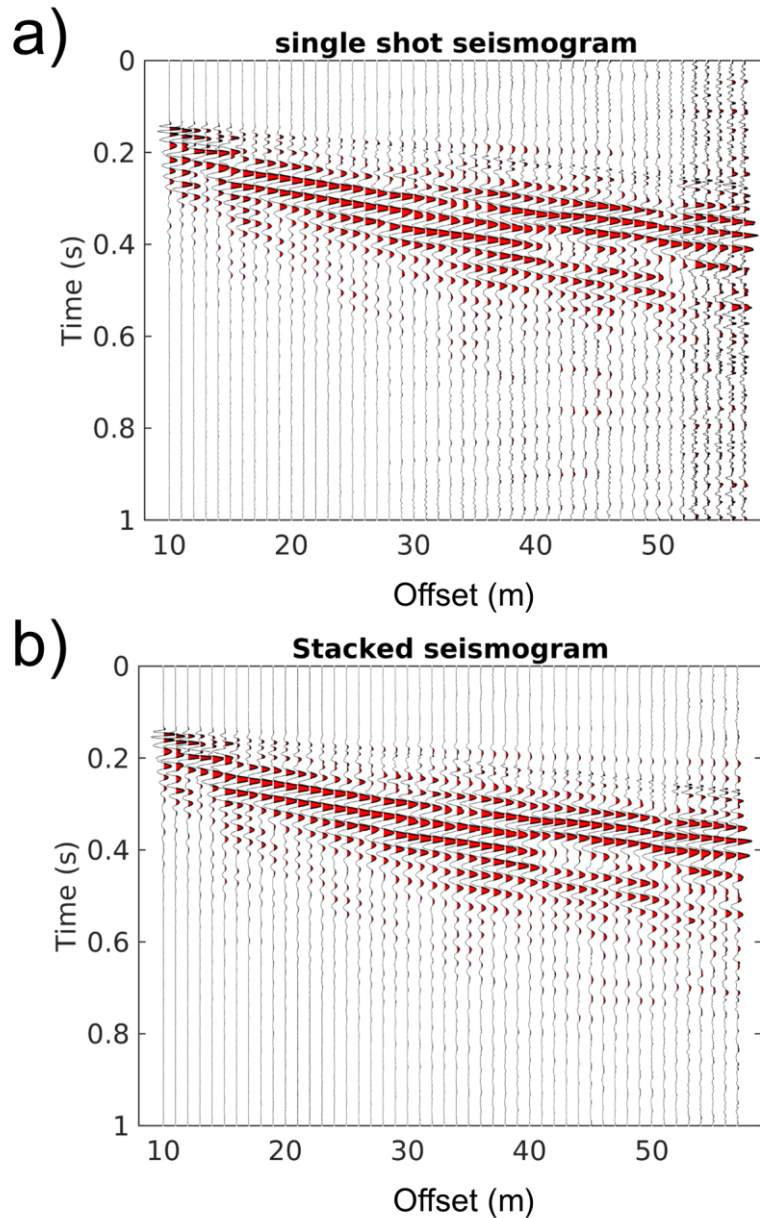
Figure A3 – a) single shot seismic section acquired having positioned the source in src1. b) Corresponding stacked seismogram (every trace is the sum of 10 different recordings).

A1.3 Processing

A1.3.1 Pre-processing

Seismic traces generated by different shots, with the source positioned at the same location (10 sets for each configuration), were summed - or stacked - in time domain. This was done to enhance the coherent seismic events generated by the controlled seismic source, and at the same time to minimize the uncoherent noise anyhow present in the recordings (Foti et al., 2015). "Stacked" seismic sections, with greater signal-to-noise ratio, were hence obtained (Figure A3b). Note that in the stacked seismogram in Figure A3b the influence of noise on the traces at long offset is not visible anymore (compare the traces at offset > 50 m in Figure A3a and A3b), confirming the effectiveness of the stacking operation.

A1.3.2 Refraction processing

P-wave first-break arrival times were manually picked on the stacked seismograms representing the vertical component of soil surface vibration. Figure A4a represents a sample seismic section and the identified first-breaks; the complete set of travel-time curves (one for each considered shooting position) is shown in Figure A4b. The hodocrones appear to be approximately symmetrical, i.e. the P-wave travel time depends only on the source-to-receiver distance and not on the position of the shot point. This suggests a 1D geometry (no lateral variations) for the subsurface immediately below the active seismic array.
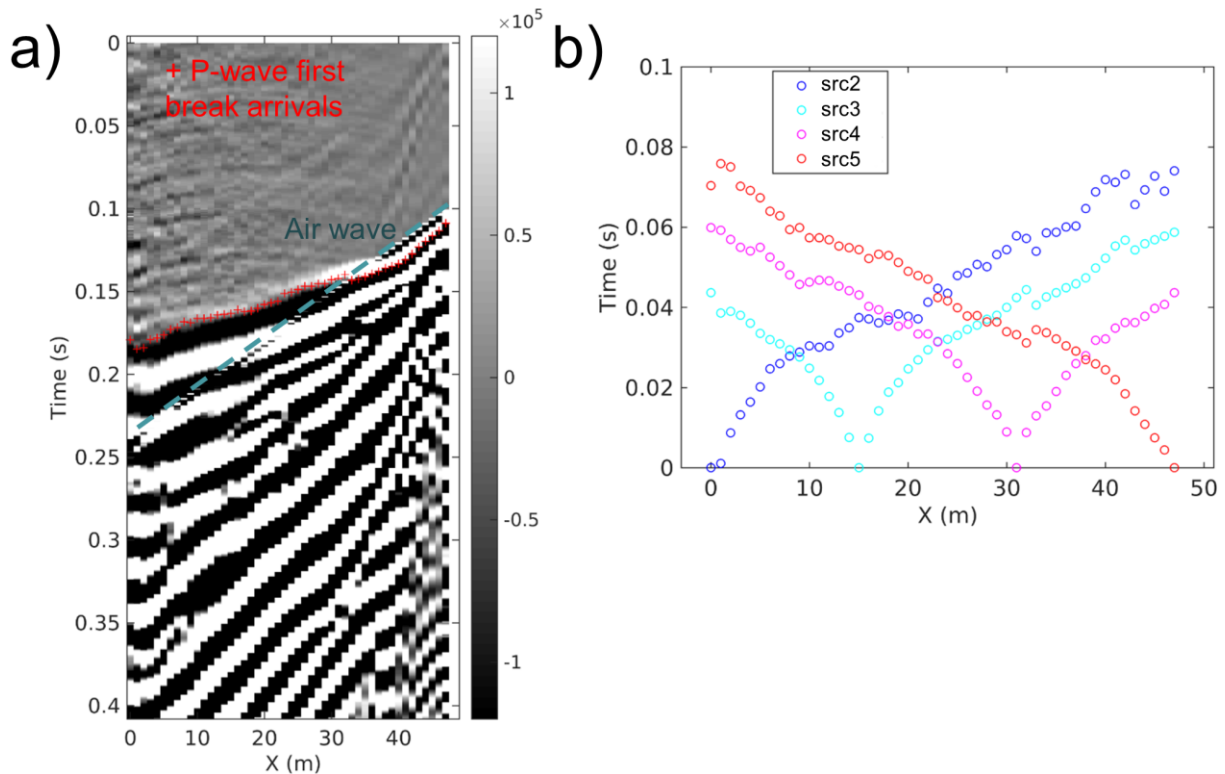

Figure A4 – P-wave refraction processing. a) Example of picking of first break P-wave arrivals (src5 stacked seismogram; b) obtained P-wave travel time curves. The X coordinate in (a) and (b) runs along the geophones spread, from its west (X = 0 m, 1st receiver) to its east end (X = 47 m, 48th receiver).

A1.3.3 MASW Processing

The stacked seismic sections acquired with MASW configuration (src1 and src6) were processed by means of a 2D *f-k* (frequency – wavenumber) transform (Socco and Strobbia, 2004), in order to obtain a conversion of the recorded sets of traces from time–offset to frequency–wavenumber domain. The energy maxima corresponding to the Rayleigh wave dispersion curves were picked on these panels (Figure A5a,b; Socco and Strobbia 2004, Foti et al., 2015).

6

The dispersion curves appear to be composed of few modal branches (Figure A5a): one (later identified as fundamental mode) extends almost continuously in a 5-50 Hz frequency band, with phase velocities within 100-300 m/s; other dispersive events, with higher velocities (200 - 400 m/s) are limited to a narrower frequency interval (20-50 Hz).

In order to attribute the obtained data points to defined Rayleigh wave propagation modes, a preliminary inversion was run with the use of the Maraschini and Foti (2010) Monte Carlo inversion tool. The code performs a purely random search in the parameters space, using as misfit function the values of the absolute determinant of the transfer matrix evaluated at the frequency-phase velocity coordinates of the experimental data points. Hence, the code does not require mode numbering but it attributes itself the experimental points to a given mode, looking for the lowest misfit solution.

The best fitting absolute determinant surface, out of a total population of $5 \ 10^5$, is shown in Figure A5c. The experimental data points actually fall in the "valleys" of the determinant surface, thus fitting the corresponding Rayleigh wave mode. These points are hence attributed to the appropriate Rayleigh wave mode, from the fundamental to the second higher mode (Figure A5d). We highlight here that the mode identified as fundamental presents a hump at circa 15 Hz; this feature is generally associated to a velocity inversion (i.e. a stiffer layer embedded within softer formations) in the subsoil. Finally, the dispersion curves from src1 and src6 recordings were merged in a single, comprehensive curve (as already shown in Figure A5d).

It is worth remarking that the Rayleigh wave dispersion curve from active data processing match quite well the phase velocities of the Rayleigh wave fundamental mode from passive data recordings in a 5-15 Hz frequency band of overlap (Figure A5b).
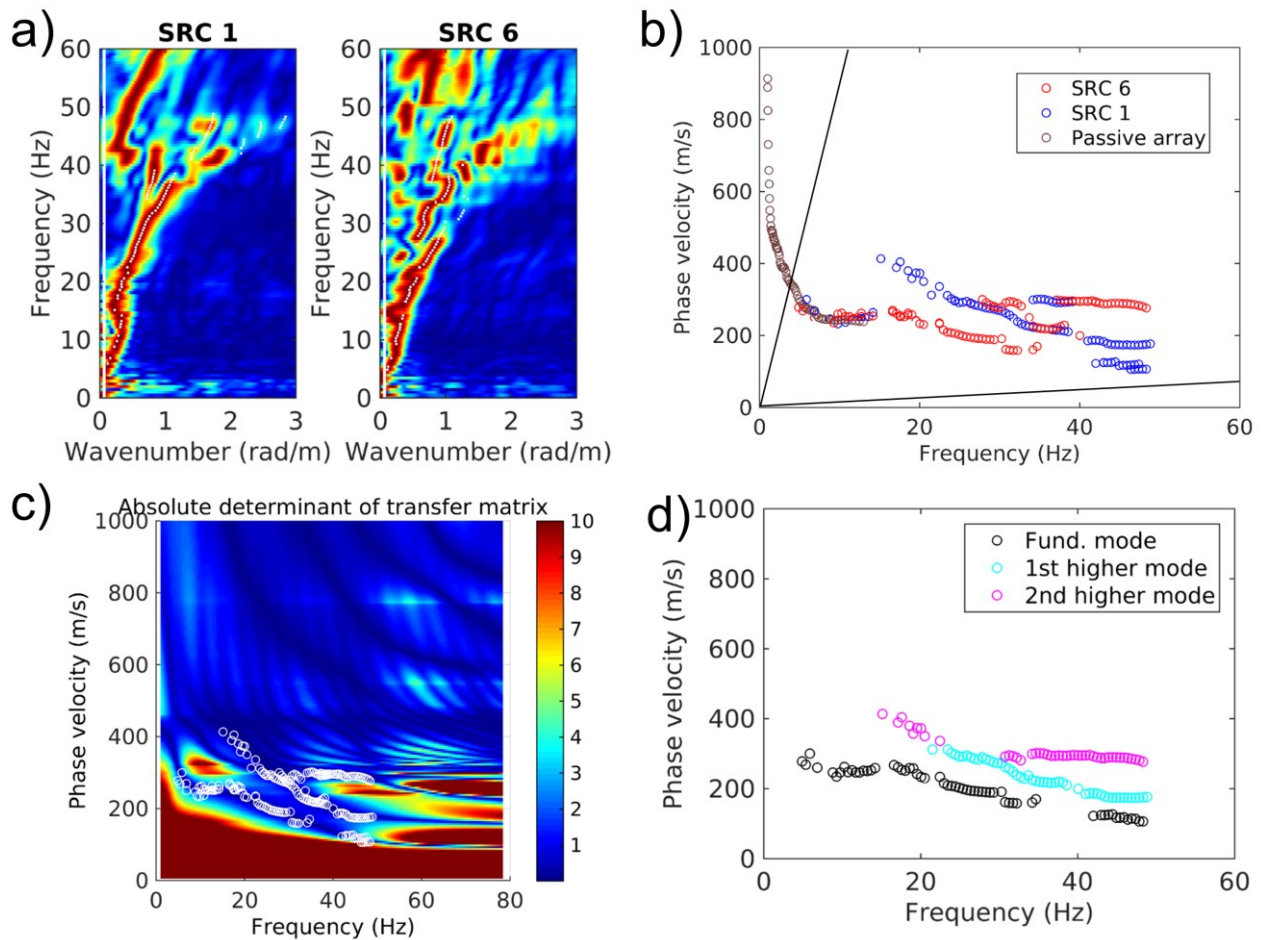
Figure A5 – a) f-k spectra obtained from the stacked seismic sections with source in src1 and 2. The picked maxima are represented as white dots. b) Obtained dispersion curves (red and blue circles) collated with the Rayleigh wave fundamental mode from passive data processing (brown circles, section 5.2). The resolution limits for the active array are represented as black lines. c) best fitting absolute determinant surface; fitted data points are represented as white circles. d) Identified Rayleigh wave modes in active array dispersion curve.

A1.4 P-wave refraction interpretation.

Refraction data (A1.3.2) were interpreted with the method of intercept time analysis (Reynolds, 2011). Following the hypothesis of a 1D geometry for the shallow subsurface (A1.3.2), the hodocrones obtained from refraction processing (Figure A4b) were collapsed into a single travel-time curve in time-offset domain (black circles in Figure A6a).

P-wave travel times follow a bi-linear trend, with direct arrivals (offset < 5 m) showing a velocity for the surficial layer of 205 m/s; the slope of the hodocrones then gradually decreases at 5 < offset < 10 m, modelled as a transition layer with V_P = 465 m/s; at offset > 10 m, P-wave arrivals bear a slope corresponding to a velocity of 875 m/s, this being the deepest layer identifiable with refraction interpretation. Figure A6b shows the identified V_P profile.
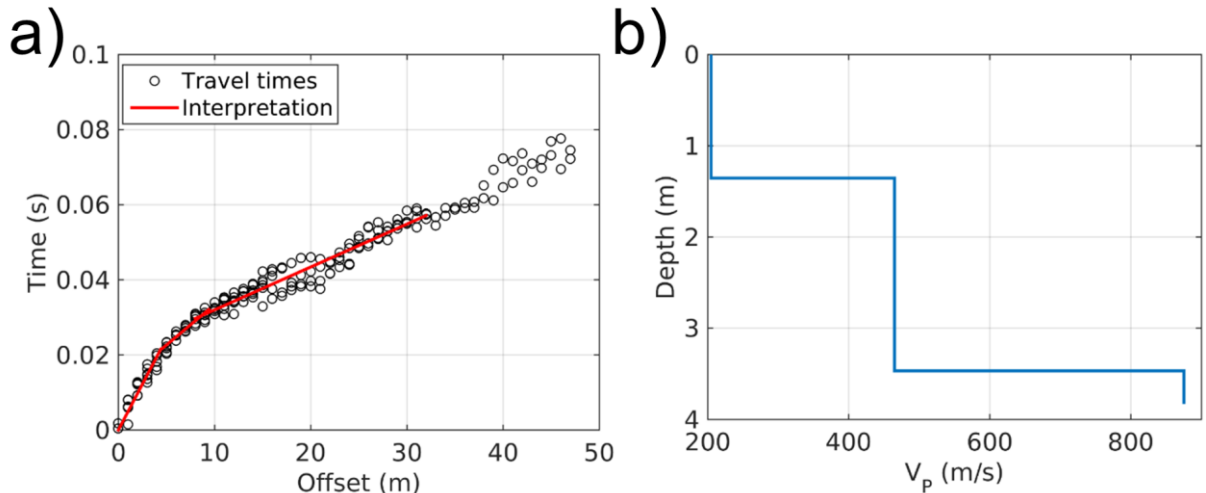
Figure A6 – P-wave travel time interpretation

A2 Rayleigh Wave Data Inversion

The objective of the inversion was determining a detailed V_S velocity profile for the shallow subsurface (first 30 m) for comparison with CPT data. With this aim, the retrieved multimodal dispersion curve (Figure A5d) was joined with Rayleigh wave data (both phase velocity and ellipticity curves for the fundamental mode) from passive data processing (section 5.2): these were considered down to a frequency of 2.2 Hz, which corresponds to a quarter-wavelength depth of 30 m (section 6.3).
The inversion was performed using the Dinver software of the Geopsy suite that implements an Improved Neighborhood Algorithm (Wathelet, 2008).

A2.1 Parameterization of the model space

The subsurface was parameterized as a set of eight stacked layers. The relatively high number of layers was made necessary to model, in a limited depth range:
- A complex surficial geometry (three layers in the first 3.5 m), as indicated by P-wave refraction (A1.4);
- A velocity inversion (as suggested by the shape of the Rayleigh wave dispersion curve, see Figure A5).
- The presence of a shallow water table, with the need to model the transition between partially and fully saturated formations (with consequences on the assumed Poisson's ratio and V_P ranges).

In fact, the geographical position of SINS station (in the strip of land between the Brienzersee and Thunersee) suggests a shallow depth of full saturation: well data from the Géoportail of Canton Bern (Géoportail du Canton de Berne, 2017) confirm this hypothesis and mark the position of the water table at the date of the survey at few meters depth. Nevertheless, the water table could not be identified through P-wave travel-time interpretation (A1.4); therefore, it was argued that this is located slightly

9

below the deepest resolved interface (at 3.5 m: see Figure A6; see section A3.2 for a discussion regarding the water table level).

Velocities and thicknesses of the first two layers (and the velocities for the third layer) were constrained to the results of P-wave refraction; as for the deepest layers, their parameters were left free to vary within wider ranges.

Taking into account the available information on the water table depth (see above), layers 3-7 were assigned Poisson's ratio (0.4 – 0.49) and P-wave velocity intervals (1400 -1900 m/s) compatible with the condition of a fully saturated granular formation. Despite the commonly assumed poor sensitivity of Rayleigh wave dispersion data towards the V_P subsurface model (Xia et al., 2003), some studies have highlighted that the contemporaneous inversion of multiple modes can actually help resolving both V_S and V_P profiles (Ernst, 2008; Bergamo and Socco, 2016). As the dispersion curve being inverted comprises the fundamental and two higher modes (Figure A5), it is reasonable to expect some sensitivity towards the depth of full saturation. As for the halfspace layer, Poisson's ratio and V_P were left free to vary in wide intervals (compatible with the conditions of partially and fully saturated formation), similarly to V_S.

A2.2 Inversion results

Adopting the constrained parameterization introduced in the previous section, an inversion run over $5 \cdot 10^5$ subsurface models was performed. The obtained velocity profiles (top panels in Figure A7) follow a consistent trend. V_S increases significantly in the first few meters of depth, from 100 m/s to around 450 m/s at 4.5 depth m. This stiff layer ($V_S \approx 450$ m/s) is quite thin, as its lower interface is placed at approximately 7 m depth. The water table probably lies within this formation, as the interface between partially ($V_P \approx 875$ m/s) and fully saturated material ($V_P \approx 1630$ m/s) is identified at approximately 6 m depth.

Between 7 and 10.5 m depth, V_S has quite lower values (around 250 m/s), marking a sharp velocity inversion with respect to the shallower layer; further below (10.5 – 31 m) S-wave velocities are slightly faster (280-320 m/s), until the upper interface of the halfspace is met ($V_S = 450$ m/s).

The overall agreement between experimental and simulated curves can be considered as good (Figure A7b). Indeed, the consistency is better for phase velocity data, than for ellipticity. Nevertheless, as far as the fitting of ellipticity data is concerned, this latter inversion for the shallow subsurface, combining active and passive surface wave data, achieves a significant improvement, when compared with the results of the inversion involving data from passive surveys only (compare Figure A7b, bottom panel, with Figure 13, upper right panel).
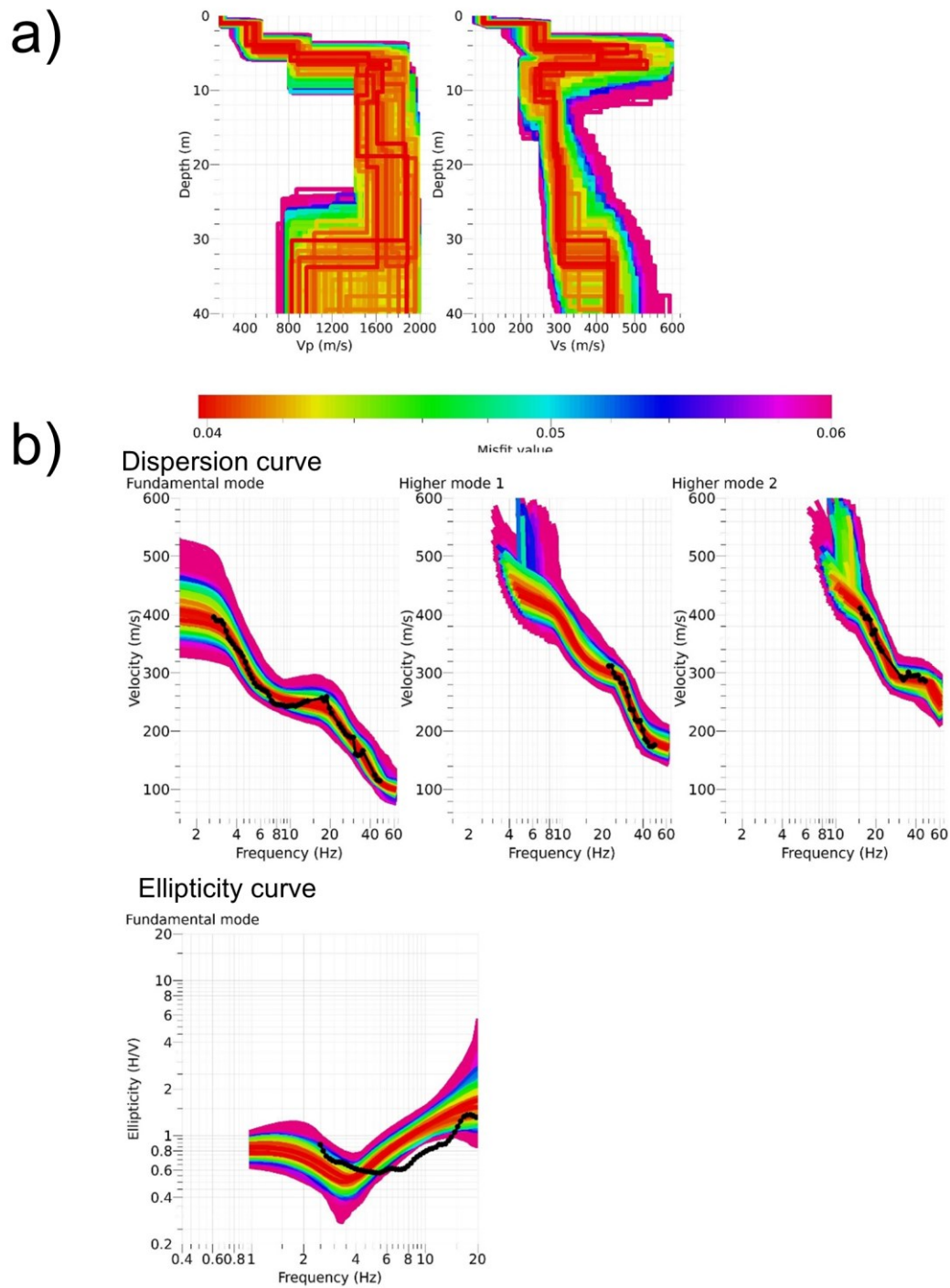
Figure A7 – Inversion results. Top: ground profiles. Centre and bottom: fitting between experimental and synthetic data.

A3   Interpretation of the velocity profiles

The 20 best performing models were extracted from the population of tested profiles and they are represented in Figure A8. The obtained V_P/V_S model is discussed in this section and collated with the data from the CPT test.
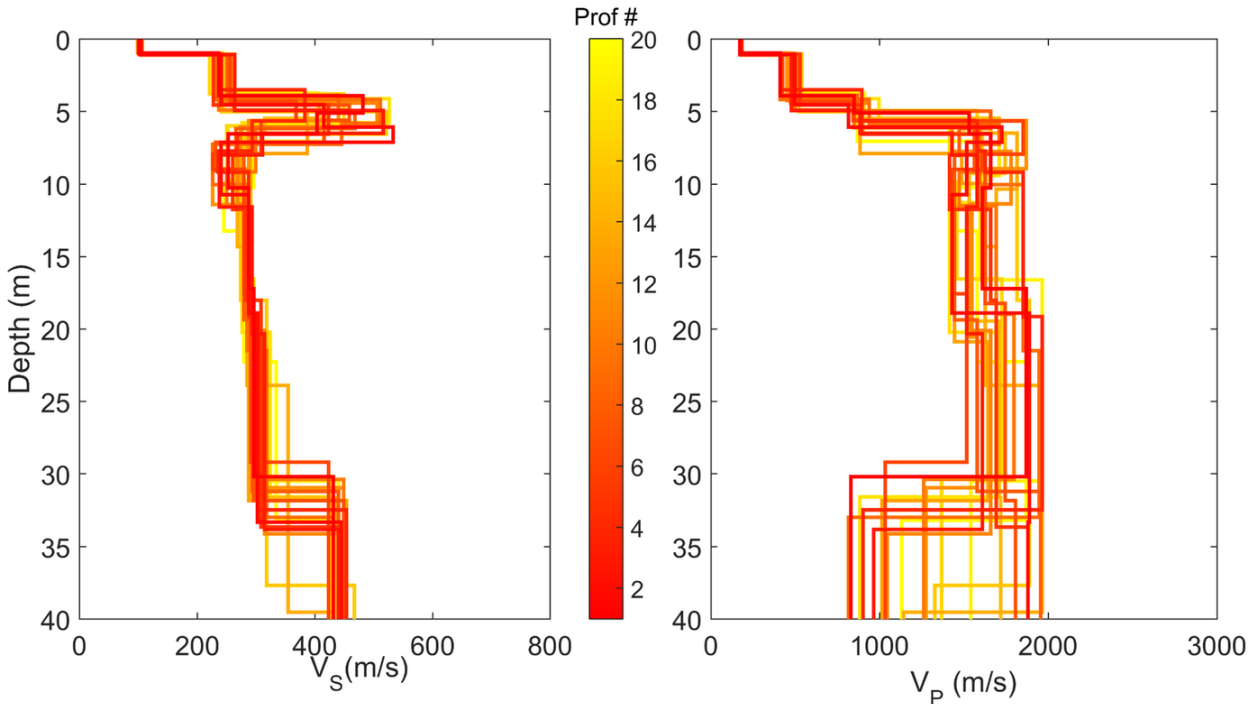
Figure A8 – Inversion results. V_S and V_P profiles from the 20 best performing models

A3.1 Stratigraphic interpretation of the velocity profiles, comparison with penetrometric data

The deepest point reached by the CPT survey was 18 m; at that depth a layer rich in stones was met, making it impossible to resume the measurement. In Figure A9, the shallower portion (first 20 m) of the V_S,V_P profiles obtained from Rayleigh wave data inversion is collated with the geotechnical log (upper left panel) and the raw data from the CPT survey (static and dynamic cone tip resistance, sleeve friction, pore water pressure: q_c, q_d, f_s and u2 in the upper right and lower left panel).

In general, there is a good agreement among velocity profiles, geotechnical log and the data collected by the CPT probe.

The two shallowest layers from seismic data inversion ($V_S = 100$ and 240 m/s) fully corresponds to a clayey and a sandy formation, respectively, identified in the geotechnical log; below, a dense gravelly layer with stones has high V_S (450 m/s) in its upper portion, decreasing to 300 m/s in the lower half. The water table is probably located within this gravel layer; see next subsection for a detailed discussion.

The low velocity area ($V_S = 250$ m/s) between 7 and 10.5 m depth matches a stack of thin clayey/sandy layers; below, the stratigraphic log again indicates a formation composed by compact gravel and stones, with lenses of silt and sand: the corresponding V_S is around 290 m/s.

The CPT data (q_c, q_d, f_s) correlate quite well with the identified V_S profile, as an increase in the penetrometric parameters corresponds to higher S-wave velocities, and vice versa "slower" layers have lower values of q_c, q_d, f_s (in agreement with literature findings: Sykora and Stoke, 1983; Baldi et al. 1989; Hegazy and Mayne 1995; Mayne and Rix, 1995; Piratheepan, 2002; Mayne, 2006; Andrus et al., 2007; Robertson, 2009). We remark in particular: the correlation between the trend

over depth of penetrometric parameters and the position of the lower interfaces of the two shallowest layers from V_S/V_P models; the peak of q_c at 3.5 – 7 m depth corresponding to sharp increase in V_S; the depth interval (8.4 – 10.3 m) with low values of q_c, f_s matching a layer with slow V_S. On the other hand, the peak in q_c, q_d at around 11 m does not correspond to any particular feature in the V_S profiles: therefore it could be ascribed to a local anomaly (e.g. a stone or boulder met by the CPT probe).

A3.2 Depth of the water table

Unfortunately, the CPT test in the depth interval 5.5 – 8 m had to be conducted by ramming a CPT cone without pore water pressure sensor, due to the stiffness of the compact gravel layer. Therefore, there is no available pore pressure measurement that could reliably identify the depth of the water table (Figure A9b, left panel). In the attempt to obtain an estimate, we computed a linear regression on the positive values of pore water pressure available in the 8 – 11 m depth range. In fact, once the water table is met by the probe, the measured water pressure (u) should linearly increase with depth (z) as:

$$u = \rho_w g(z\text{-}z_w)$$
ρ_w = water density
g = gravity acceleration
z_w = water table depth

although the linear trend might be disturbed by local overpressure or suction phenomena.

The 0 intercept of the performed linear regression (corresponding to z_w) is at 4.9 m, not far from the interface between partially and fully saturated layers identified in the surface wave data inversion (6 m; see Figure A9b). These two estimates for the depth of the water table are compared with well data from the area of Interlaken (Figure A10; Géoportail du Canton de Berne, 2017). The two measuring stations closest to SINS place the water table at an elevation of 562.5 (G268, west of SINS) and 565.6 m (G270, south of SINS) on 03.03.2017 (active seismic acquisition), and of 563.8 and 565.8 m on 10.03.2017 (execution of CPT survey). The estimates we obtained for the water table depth (Figure A9b) are compatible with well G268 data (5.2 – 3.9 m), but exceed the measurements from G270 (2.1-1.9 m). In any case, it is worth highlighting the remarkable spatial and temporal variation in the groundwater level measured at the two wells; the latter (temporal variability) could explain the difference in the estimates obtained from seismic survey (performed on 03.03.2017) and CPT data (10.03.2017).
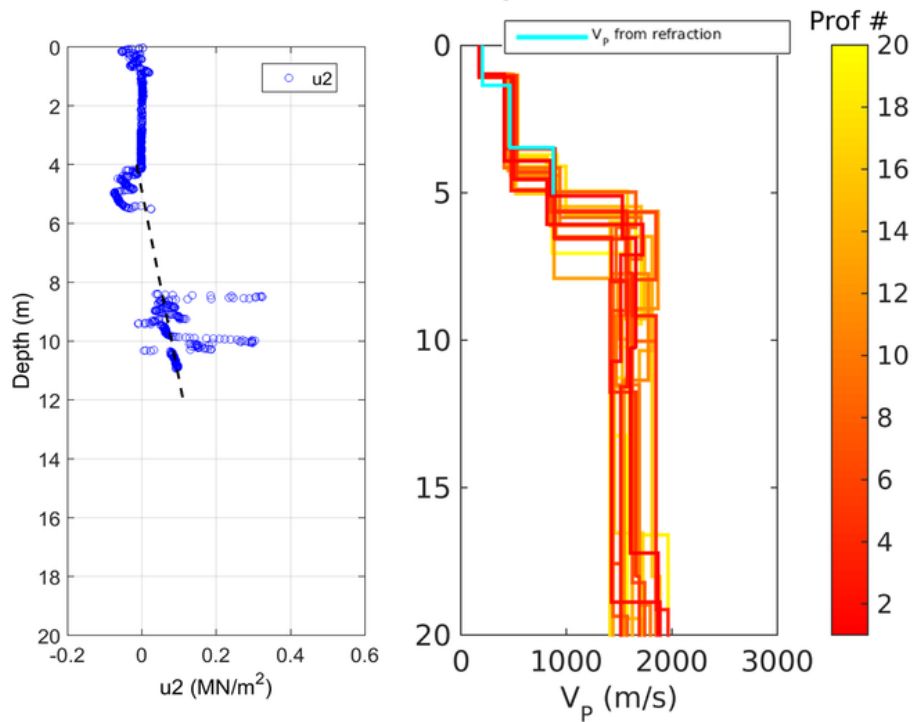
13
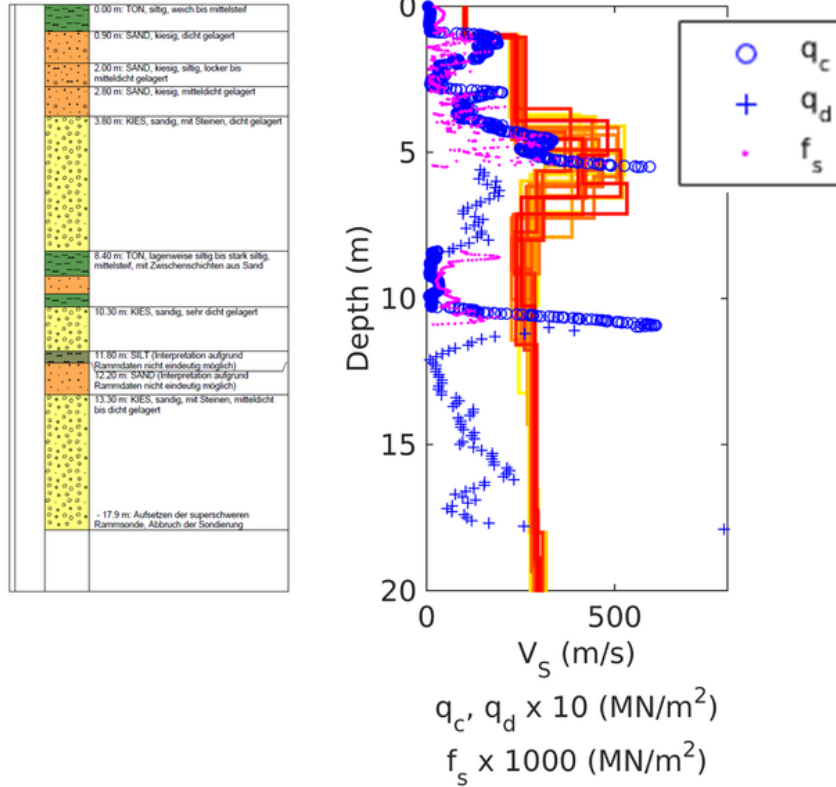
Figure A9 – Comparison between CPT and Rayleigh wave inversion results. a) stratigraphic log from CPT survey (left panel) and 20 best V_S profiles from Rayleigh wave data inversion (right panel), In the same panel, the sleeve friction (f_s), static (q_c) and dynamic (q_d) cone tip resistance from CPT survey are also represented. b) pore water pressure measured in CPT survey (blue circles) and linear regression over its positive values (depth range 8 – 11 m) in the attempt to estimate the water table depth (right panel); V_P profiles from the 20 best performing models and V_P stratigraphy from P-wave refraction interpretation.
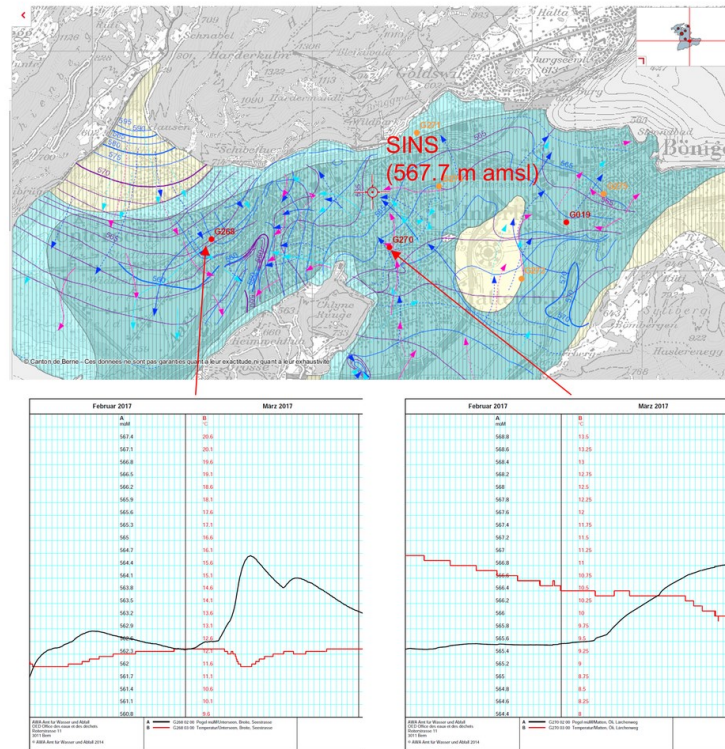
Figure A10 – Top: ground water map of the area of Interlaken (Géoportail du Canton de Berne, 2017). The location of station SINS is indicated by a red cross. The water table depth measurements from the two wells close to SINS are displayed in the bottom panels.

The last topic worth discussing is why P-wave refraction analysis did not identify and determine the depth of the water table. In fact, the picked hodocrones align along slopes that are not compatible with that determined by a water-filled soil ($V_P \approx 1500$ m/s or greater). To ascertain whether P-wave first break arrivals had been misidentified during picking, we computed the theoretical travel time curve that would be obtained with a P-wave model similar to that in Figure A6b, adding a layer of saturated gravel ($V_P = 1620$ m/s) at a depth of 6 m (as obtained from Rayleigh wave data inversion, Figure A8b). The computed synthetic hodocrone was superimposed to the seismograms where the picking was performed (Figure A11a), and on the whole set of experimental travel time curves (Figure A11b). In both cases, there are hints suggesting that P-wave actually follow the computed hodocrone (green line), at an offset of 15 – 25 m. However, these arrivals are not clearly visible (this might be due to the fact that P-waves refracted along the surface of a solid-liquid matrix have lower amplitude than those refracted on a solid-solid interface).

To conclude, gathering all the pieces of information presented in this subsection, the most likely estimate for the water table level is slightly below the upper interface of the shallow gravel layer (~3.5 – 4 m, Figure A9) and within this formation, probably at a depth of 4 – 6 m.
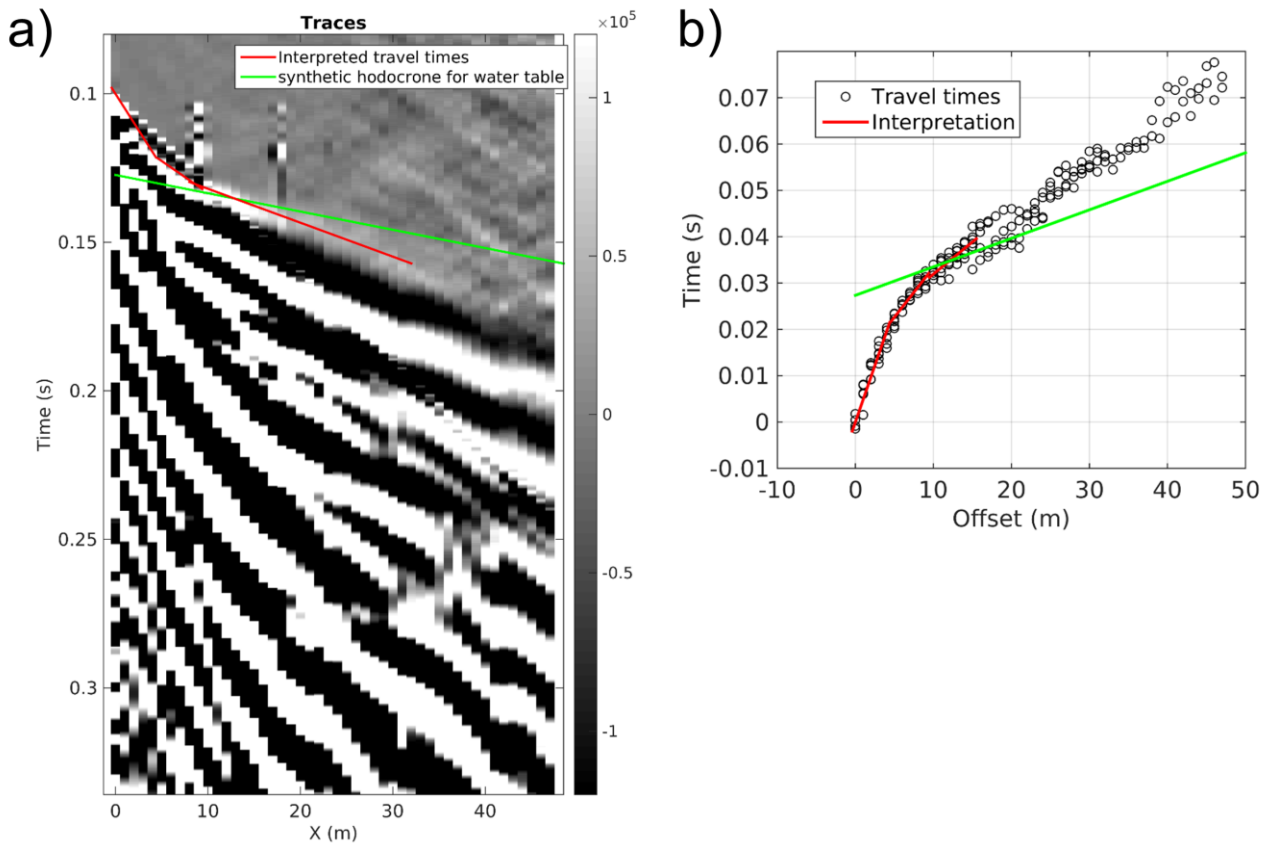
Figure A11 – Synthetic P-wave hodocrone for a water table at 6 m depth (green line), superimposed to a seismic section (a) and to the whole set of P-wave travel-times (b).

A3.3 Comparison with the inversion of passive surface wave data

We compare the results obtained here from the inversion of active and passive Rayleigh wave data for a shallow subsurface model (section A2) with the velocity profiles determined from the inversion of passive surface wave data alone (section 6). The comparison is displayed in Figure A12. As for V_S profiles (Figure A12, left panel), the most evident discrepancies are the difference in the estimation of the velocity of the second layer, and the lack, in the passive data inversion, of the stiff lens at 3.5 − 7 m. Below this layer, the profiles from passive data inversion slightly overestimate V_S; the two sets of models finally agree in placing an interface at ∼ 33 m, and in defining the S-wave velocity of the formation below (∼450 m/s). Indeed, the inclusion of high frequency active surface wave data has enabled a more reliable and detailed description of the shallower subsurface; nevertheless, the estimation of the V_{S30} seem to be poorly affected by this additional information (the difference between the two V_{S30} estimates is only 4 m/s).

As far as V_P profiles are concerned (right panel), the main difference is the depth range 7 − 33 m, where the inversion of active and passive data forces P-wave velocity to assume values compatible with saturated granular materials (following available geological information). At ∼ 33 m depth, the two sets of lines match by aligning around a V_P of 1000 m/s.
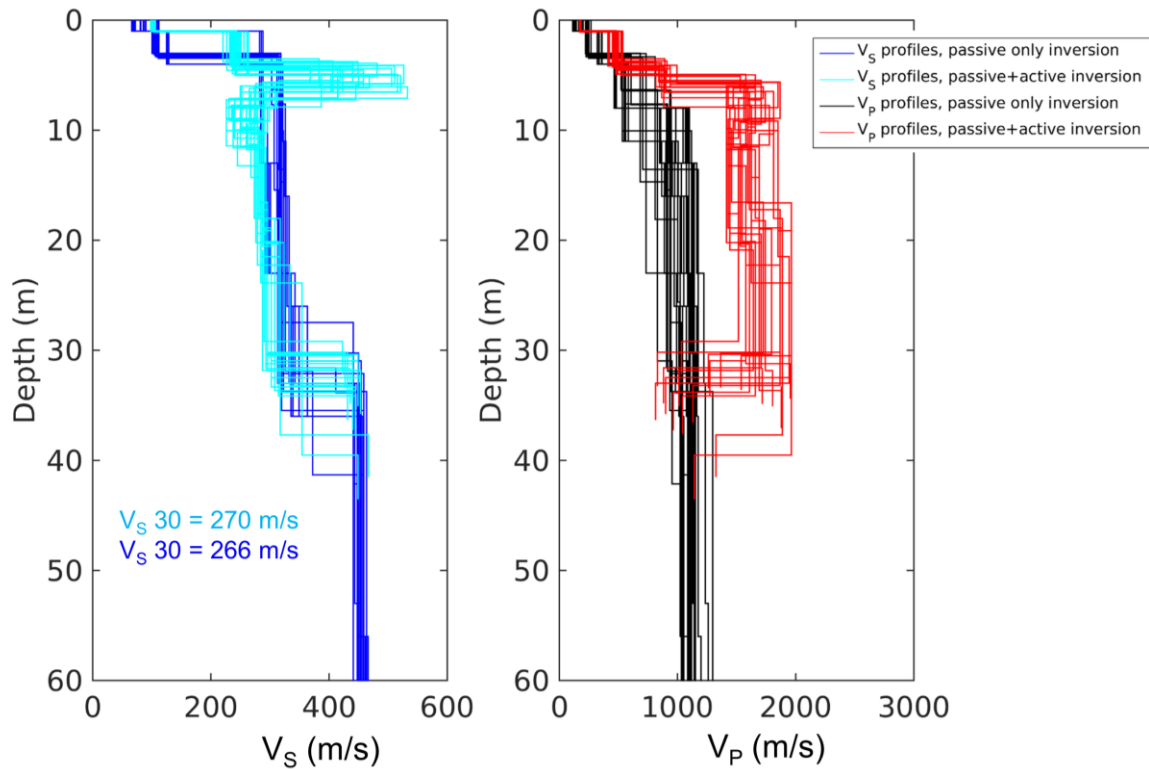
16

Figure A12 – Comparison between the best performing models obtained from the inversion of surface wave passive data alone (blue and black profiles, section 6) and from the inversion of active and passive data for a shallow subsurface model (cyan and red profiles, section A2).

A4 Combining the results of active and passive survey

Due to time constraints it was not possible to re-run the whole inversion process, assuming as input data a Rayleigh wave dispersion curve combining the complete branches from active and passive surveys (Figure A5b). However, considering the continuity between the velocity profiles from the two inversions around the lower investigation depth of the active measurement (circa 30-40 m; Figure A12), these two sets of profiles were merged so to produce a more complete description of the subsurface at SINS site. Understandably, the velocity profiles from the active measurement cover the shallow 30-40 m; below, the models from the passive data-only inversion (Michel et al., 2013, section 6.1) were kept unchanged. The best performing 25 models from the MASW survey were joined with the 25 best profiles from the passive-only measurement (see Figure 15 of passive survey report, Michel et al., 2013). The pairs of models were defined identifying the profiles with the minimum velocity difference at the layer having its upper interface at 30-40 m depth (Figure A12), considering both V_P and V_S. As final result, we have a set of 25 velocity models (Figure A13) having either 11, 13, 16, 18 or 20 layers. The upper 7 layers are drawn from the profiles resulting from the active data analysis; they replace the original shallower formations from the passive data-only inversion.
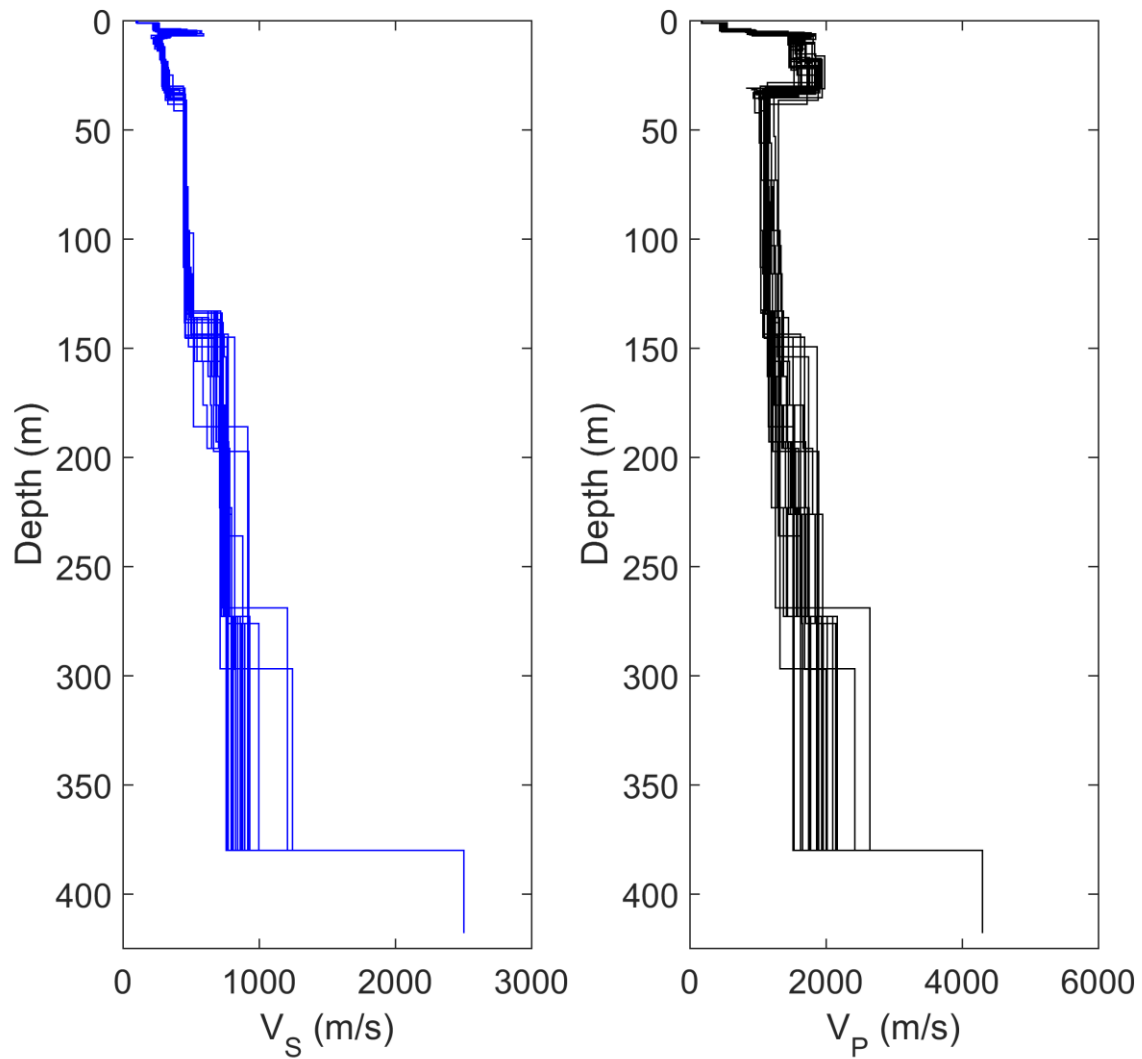
Figure A13 – V_S and V_P profiles obtained joining by pairs the 25 best performing models from the active and passive data analysis.

The match between the synthetic ellipticity and dispersion curves from the obtained velocity models (Figure A13) and the experimental curves from active and passive data analysis was verified; the comparison is displayed in Figure A14. The fit at low frequency is similar to that obtained from the passive data-only inversion (see Figure 13 and section 6.1 in Michel et al., 2013), meaning that modifying the shallow part of the velocity models has not compromised the data fit.
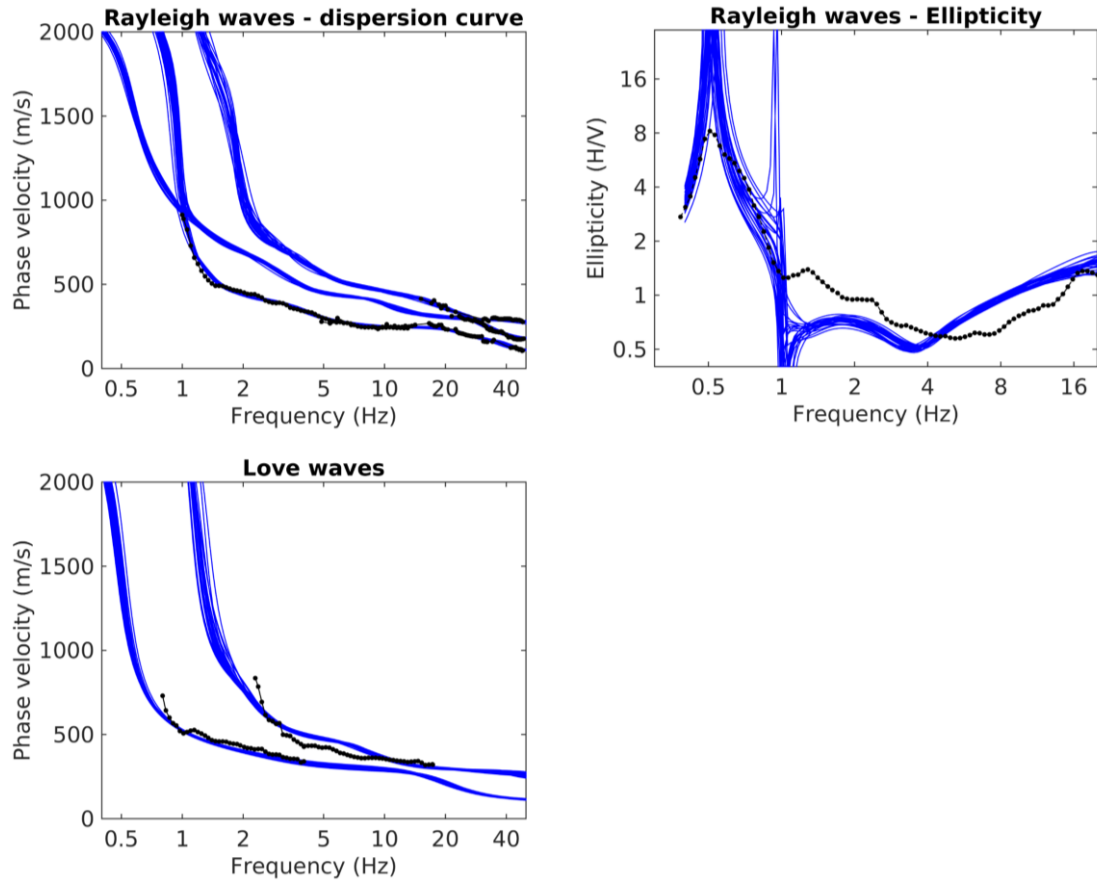
Figure A14 – Fitting between experimental curves (from passive and active surface wave surveys, black lines) and synthetic dispersion and ellipticity curves (blue lines) from the models obtained combing the velocity profiles from the passive data-only processing and the active+passive Rayleigh wave dispersion curve inversion (this appendix). Note that the adopted axis limits make these plots comparable with those of Figure 13 in Michel et al. (2013).

A4.1 Quarter-wavelength representation

The quarter-wavelength velocity representation (Vs^{QWL}; Joyner et al., 1981) attributes to each frequency the average velocity at a depth equal to ¼ of the corresponding wavelength. Vs^{QWL} can be used as direct proxy for the local site characterization, as it physically relates the resolution on ground parameters with the characteristics of the propagating wave-field at the discrete frequencies. The derived quarter-wavelength impedance contrast (IC^{QWL}; Poggi et al., 2012) is the ratio between two quarter-wavelength average velocities, from the top and bottom part of the velocity profile respectively, at a given frequency; it is a powerful tool to assess the influence of resonance phenomena in soft sediment sites.

Figure A15 shows the average (over the population of the 25 subsurface models derived in the previous paragraph, Figure A13) quarter-wavelength velocity (centre) and impedance contrast (bottom) representations. The obtained Vs30 (which is the average velocity corresponding to a quarter-wavelength of 30 m) is 270 m/s.

The IC^{QWL} graph shows the right flank of a peak at 0.5-0.8, which is related to upper interface of the identified halfspace at 380 m depth (lower end of the sedimentary cover). Another peak is at 25 Hz, and it corresponds to the sharp velocity increment at the shallow layers.
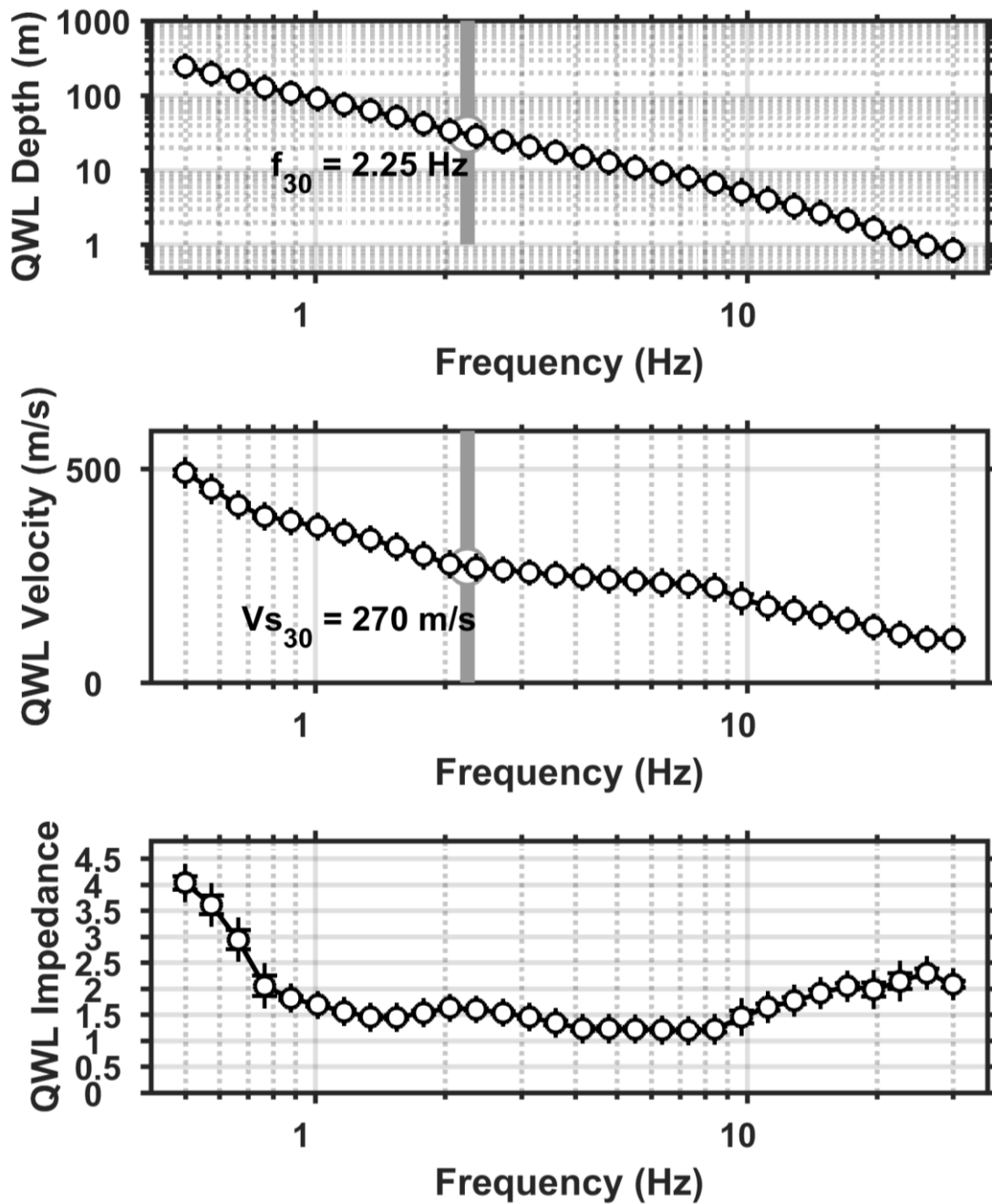
Figure A15 – Average quarter-wavelength representation of the derived velocity profiles (Figure A13). Top: depth; center: velocity; bottom: impedance contrast. The gray line in the top and center panel refers to Vs$_{30}$.

A4.2 SH transfer function.

The theoretical SH-wave transfer functions for vertical propagation (Roesset, 1970) were computed for the reconstructed models (Figure A13). The transfer functions are then corrected for the Swiss reference rock model (Poggi et al., 2011), following Edwards et al. (2013).

Their average (black line in Figure A16) is compared with the empirical amplification function obtained from spectral modeling (ESM, Edwards et al., 2013; Michel et al., 2014), relying on 45 or more events in the central $1 - 7$ Hz frequency band, decreasing down to 1-5 events at lower and higher frequencies (as of 04.04.2018). The modeled function reaches in general lower amplification values when compared to the empirical curve. Nevertheless, the synthetic curve manages to reproduce the main features of and empirical function: the peak at 0.5 Hz (related to impedance contrast between the sedimentary cover and the lower rock formation at 380 m depth), and the two peaks at high frequencies (15 and 30 Hz), which should correspond to the sharp increment in V_S in the very shallow subsurface (the 15 Hz peak, in particular, is to be associated with the stiff formation reaching $V_S = 450$ m/s at around 5 m depth).

In Figure A17 we include also the average modeled SH transfer function from the 25 best models from the passive data-only inversion (red line): not surprisingly, this fails to reproduce the high frequency peaks of the empirical amplification function, as the corresponding velocity profiles lack a detailed reconstruction of the shallow subsurface.
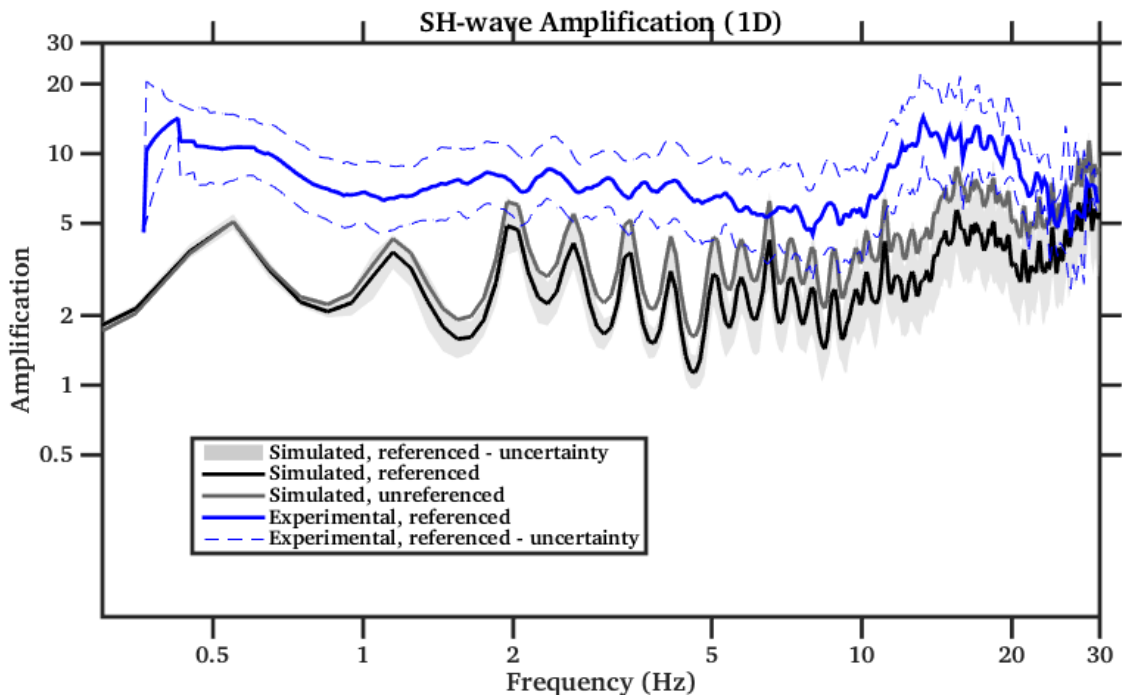

Figure A16 – Average SH transfer function for the reconstructed velocity models in Figure A13 (gray line), also referred to the Swiss reference rock (black line). In blue, the empirical amplification function from spectral modeling, referred to the Swiss reference rock.
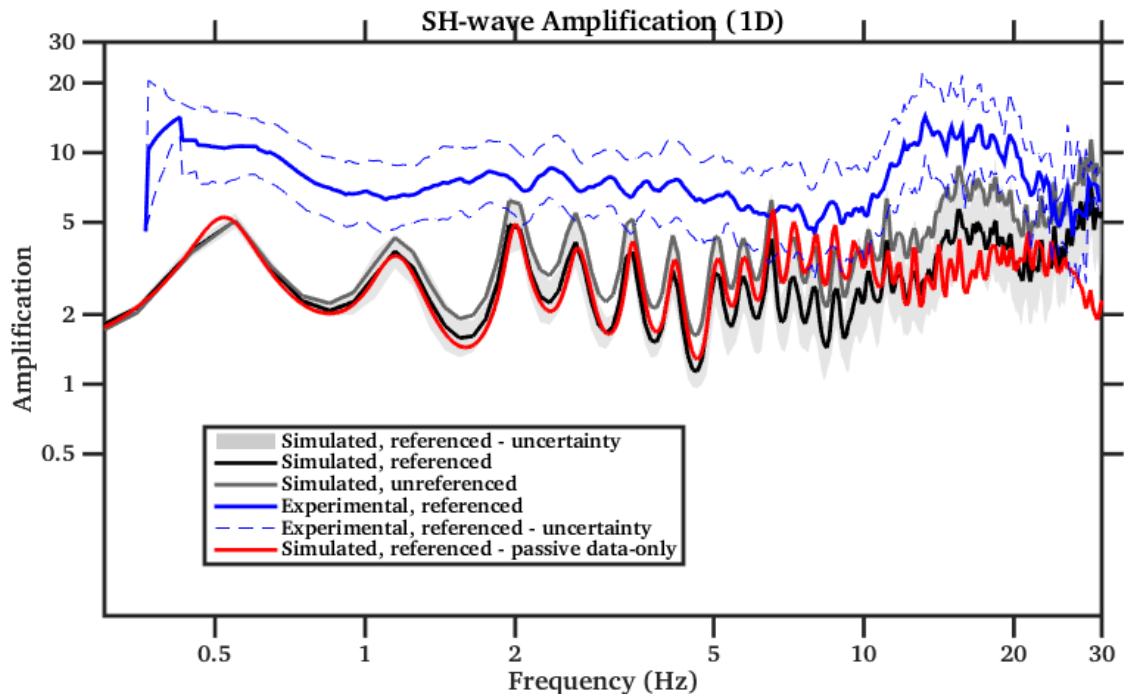
Figure A17- Same as A16, with the addition of the average SH transfer function from the velocity profiles from the passive data-only inversion (red line).

A5 Conclusions

This appendix contains the results of the analysis of the active survey data acquired at SINS site in parallel with a CPT measurement, and carried out with the purpose of reconstructing in detail the structure of the shallow subsurface (first 30 m). These results are to be intended as completing the analysis of the passive data by Michel et al. (2013).

The main outcomes are:

1) the identification of a stiff (V_S around 450 m/s) lens of gravel mixed with stones at approximately 5 m depth; this layer is embedded in softer sandy, clayey and silty formations, whose S-wave velocity (circa 300 m/s) is slightly slower than that determined with the use of passive data alone;

2) The identification of the depth of the water table (around 4 m), the upper limit of a shallow aquifer probably extending to 30-35 m depth.

The inversion process was not repeated combining the dispersion curves from active and passive measurements. Observing their agreement around the lower depth limit of the active survey (30-35 m), the shallow (30 – 40 m) portion of the velocity profiles from passive data-only was replaced with the velocity models from the analysis of active data; at larger depths (40-400 m), the original profiles from Michel et al. (2013) were kept unchanged.

The now more accurate estimation of the Vs30 is 270 m/s, only slightly higher than the value from the microtremor data analysis (266 m/s). The soil classification for site SINS remains therefore unchanged (class D for SIA-261, class C for Eurocode 8).

The inclusion of the detailed near-surface models in the final velocity profiles allows modeling the high frequency peaks (15, 30 Hz) of the empirical amplification function.

Appendix A - References

Andrus, RD, NP Mohanan, P Piratheepan, BS Ellis, and TL Holzer (2007). Predicting shear-wave velocity from cone penetration resistance, Proc., 4th Inter. Conf. on Earthq. Geotech. Eng., Thessaloniki, Greece

Baldi, G, R Bellotti, VN Ghionna, M Jamiolkowski, and DCF LoPresti (1989). Modulus of sands from CPTs and DMTs, Proc., 12th Inter. Conf. Soil Mech. and Foundation Eng., Vol. 1, Rio de Janeiro, pp. 165–170.

Bergamo, P. and L.V. Socco, 2016 P- and S-wave velocity models of shallow dry sand formations from surface wave multimodal inversion. Geophysics 81(4):R197-R209

CEN, 2004. Eurocode 8: Design of structures for earthquake resistance – Part 1: general rules, seismic actions and rules for buildings. European Committee for Standardization, en 1998-1 edition.

Edwards, B., Michel, C., Poggi, V., and Fäh, D., 2013. Determination of Site Amplification from Regional Seismicity: Application to the Swiss National Seismic Networks. Seismological Research Letters, 84(4).

Ernst, F.E., 2008. Multi-mode Inversion for P-wave Velocity and Thick Near-surface Layers. Extended abstract A13, Proceedings of EAGE Near Surface 2008.

Foti, S., Lai C.G., Rix G.J., and C. Strobbia, 2015, Surface Wave Methods for Near-Surface Site Characterization: CRC Press, Taylor & Francis Group LLC

Géoportail du Canton de Berne, 2017. Carte des gisements d'eau souterraine. http://www.map.apps.be.ch/pub/synserver?project=a42pub_gw25&userprofile=geo&language=fr, consulted on 11.04.2017.

Hegazy, YA, and PW Mayne (1995). Statistical correlations between VS and cone penetration data for different soil types, Proc., Inter. Symp. on Cone Penetration Testing, CPT '95, Linkoping, Sweden, Vol. 2, pp. 173–178.

Joyner, W. B., Warrick, R. E., and Fumal, T. E. (1981). The effect of Quaternary alluvium on strong ground motion in the Coyote Lake, California, earthquake of 1979. Bulletin of the Seismological Society of America, 71(4):1333–1349.

Maraschini M., and S. Foti, 2010. A Monte Carlo multimodal inversion of surface waves. GJI, 182 (3). 1557 – 1566.

Mayne, PW (2007). Cone penetration testing state-of-practice. NCHRP Project 20-05 Topic 37-14. 67

Mayne, PW, and GJ Rix (1993). Gmax-qc relationships for clays, Geotech. Testing J., 16(1):54–60.

Michel, C., V. Poggi, D. Roten, J. Burjanek, C. Cauzzi, and D. Dah, 2013. Interlaken-Schloss (SINS) – Site characterization report. Schweizerischer Erdbebendienst.

Park, C. B., R. D. Miller, and J. Xia, 1999. Multichannel analysis of surface waves: Geophysics, 64, 800–808.

Piratheepan, P (2002). Estimating Shear-Wave Velocity from SPT and CPT Data. Master of Science Thesis, Clemson University.

Poggi, V., Edwards, B., and Fäh, D. (2011). Derivation of a Reference Shear-Wave Velocity Model from Empirical Site Amplification. Bulletin of the Seismological Society of America, 101(1):258–274.

Poggi, V., Edwards, B., and Fäh, D. (2012). Characterizing the Vertical-to-Horizontal Ratio of Ground Motion at Soft-Sediment Sites. Bulletin of the Seismological Society of America, 102(6):2741–2756.30

Redpath, B. B., 1973, Seismic refraction exploration for engineering site investigations: National Technical Information Service, Technical Report E-73-4.

Robertson, P.K., 2004. Evaluating Soil Liquefaction and Post-earthquake deformations using the CPT. Proc. 2nd Geotech. Geophys. Site Charact., ISC '3, Millpress, Rotterdam, 1:233-252.

Robertson, PK (2009). Interpretation of cone penetration tests – a unified approach, Canadian Geotech. J., 46(11):1337–1355.

Robertson, P.K., R. G. Campanella, D. Gillespie, and A. Rice, 1986. Seismic CPT to measure In Situ Shear Wave velocity. ASCE J. GED, 112(8), 791-803.

Roesset, J. (1970). Fundamentals of soil amplification. In Hansen, R. J., editor, Seismic Design for Nuclear Power Plants, pages 183–244. M.I.T. Press, Cambridge, Mass.

SIA, 2014. SIA 261 Einwirkungen auf Tragwerke. Société Suisse des ingénieurs at des architectes, Zurich, Switzerland.

Socco, L.V., and C. Strobbia, 2004, Surface-wave method for near-surface characterization: a tutorial: Near Surface Geophysics, 2, no. 4, 165-185.

Sykora, DE, and KH Stokoe (1983). Correlations of in-situ measurements in sands of shear wave velocity, Soil Dyn. Earthq. Eng., 20:125–36

Wathelet, M., 2008. An improved neighborhood algorithm: Parameter conditions and dynamic scaling. GRL, 35, no.9, 1-5.

Xia, J., R. D. Miller, C. B. Park, and G. Tian, 2003. Inversion of high frequency surface wave with fundamental and higher modes. Journal of Applied Geophysics, 52, 45-57.